NANOELECTRONICS

Investigation into the transport properties of isolated FePt nanoparticles using STM

Maarten Groen

Master's thesis, June 2011

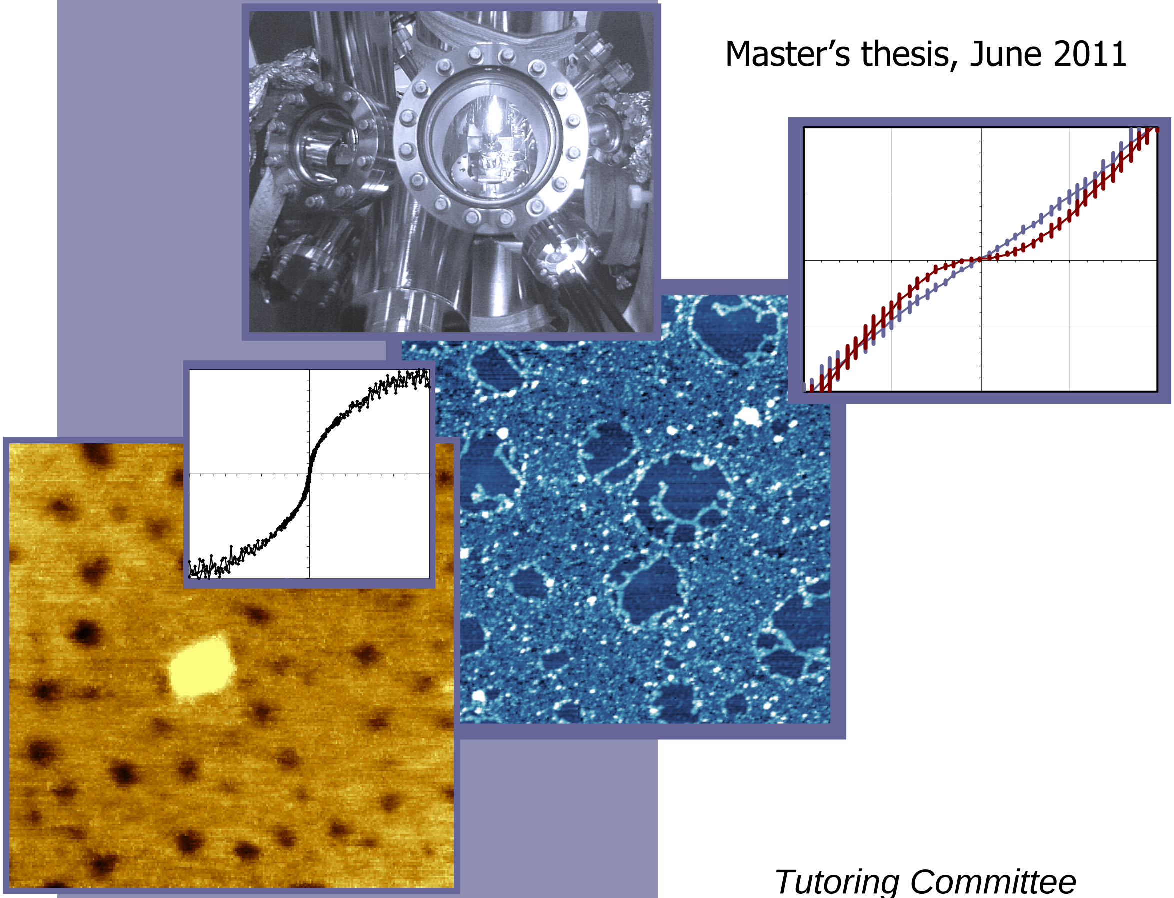

Tutoring Committee

Prof. dr. ir. Wilfred van der Wiel
Prof. dr. ir. Harold J.W. Zandvliet
Dr. ir. Michel de Jong
Ing. Martin H. Siekman
Tian Gang M.Sc.

MESA+
INSTITUTE FOR NANOTECHNOLOGY

UNIVERSITY OF TWENTE.

Investigation into the transport properties of isolated FePt nanoparticles using STM

Master's thesis of M.S. Groen

Submitted June 6th, 2011

Supervisors:
Prof. dr. ir. Wilfred van der Wiel
Tian Gang M.Sc.

Tutoring Committee:
Prof. dr. ir. Wilfred van der Wiel †
Prof. dr. ir. Harold J.W. Zandvliet *
Dr. ir. Michel de Jong †
Ing. Martin H. Siekman †
Tian Gang M.Sc. †

† NanoElectronics (NE) group, EEMCS faculty, University of Twente
** Physics of Interfaces and Nanomaterials (PIN) group, TNW faculty, University of Twente*

NanoElectronics

MESA+
INSTITUTE FOR NANOTECHNOLOGY

UNIVERSITY OF TWENTE.

Abstract

Using single, hard-magnetic clusters at the nanoscale may be an important step towards higher bit densities and improved performance for next-generation data storage systems. In light of this application, this project investigates the electron transport properties of ~3 nm FePt nanoparticles using STM spectroscopy, focusing on single-electron tunneling (Coulomb blockade) behavior and spin-dependent transport (TMR measurements).

The deposition of single, isolated nanoparticles on surfaces is studied and achieved through control of nanoparticle dispersion concentration and submergence time of adhesive substrates in this dispersion. The results are verified by STM topographic and spectroscopic measurements. For single-electron experiments highly conductive gold surfaces were fabricated, while for TMR experiments Co/Al_2O_3 and LSMO surfaces were fabricated as ferromagnetic substrates.

Particle immobilization on gold substrates is achieved using 1,9-nonanedithiol self-assembled monolayers, as demonstrated by STM topographic imaging. For Co/Al_2O_3 and LSMO substrates a ~3 nm poly(ethyleneimine) polymer film is used as adhesion layer. On this material anchoring is found to not be strong enough to allow STM measurements, and strong tip degradation is observed.

Using the dithiol adhesion layer on flame-annealed gold, the Coulomb blockade is reproducibly observed in STM I-V spectroscopy at low temperature ($T \approx 40$ K). The Coulomb staircase is used to derive a Coulomb charging energy of ~0.15 eV ($\hat{=}$ ~1.1 aF total capacitance) for one nanoparticle. The onset of Coulomb blockade is also made visible in room temperature measurements.

Table of contents

1 Motivation

Since the discovery of giant magnetoresistance (GMR) in current-in-plane (CIP) thin-film structures of alternating ferromagnetic and non-magnetic materials [1, 2], the field of spintronics has gained massive attention from researchers and industry alike. The direct application of GMR junctions in magnetic hard disk drive read heads has provided a strong push for further development of spin-sensitive electronics and the term "GMR" now appears in thousands of patents in the US alone.

Looking toward the future, incorporating ferromagnetic components into electronic structures enables the combination of electronic switching behavior and magnetic memory functionality into single devices, promising exciting new possibilities including non-volatility, increased processing speed, improved power efficiency and higher integration densities [3, 4]. Specifically the magnetoresistive random access memory (MRAM) has been in development for some time [5, 6], but although some designs have progressed to the production stage [7, 8] the miniaturization of these devices is a limiting factor in their competing with other computer memory systems.

To maintain the long-term integrity of magnetically stored data the ratio between stored magnetic energy and thermal energy should be on the order of 40 to 60, which puts a lower limit on the grain size in magnetic storage media [9]. A significant amount of interest therefore exists for the application of patterned media or self-assembled nanoparticle arrays, as data storage in isolated, monodomain particles allows for much higher storage densities than multi-granular media [10].

This research project focuses on nanoparticles comprised of an FePt alloy, which are of particular interest because they offer high magnetocrystalline anisotropy, great chemical stability compared to other common magnetic materials such as cobalt or iron, and very large scales of integration due to their reduced size [11]. Thus self-assembled monolayers of FePt nanoparticles are interesting candidates for new magnetic media, and isolated particles can be of interest in miniaturization of MRAM designs.

An FePt nanoparticle-based magnetic tunneling junction (MTJ) can offer spin-valve behavior at the nanometer scale. The small dimensions involved open a new regime of behavior where new effects can be observed and harnessed. An important example of this is single-electron tunneling, which occurs when tunneling through an electrically isolated quantum dot of extremely small electrical capacitance. Single-electron tunneling has been reported to cause an enhancement of tunneling magneto-resistance effects [12, 13, 14], which may lead to an increase in readout signal allowing higher storage densities or operating speeds.

A second concept of interest is the magnetization switching of a magnetic material using a spin-polarized current instead of a magnetic stray field. This spin transfer torque switching process has been proposed as a highly efficient and fast alternative to field writing and is particularly interesting for MRAM applications, as the abolishment of field writing allows greatly improved integration levels [15, 16].

To provide a platform for investigating these effects in FePt nanoparticles, an experimental setup is designed consisting of a scanning tunneling microscope (STM) and samples with isolated FePt nanoparticles deposited on a ferromagnetic substrate (see Figure 1.1). The double tunnel junction (STM tip, nanoparticle and substrate) is required for single-electron tunneling. TMR experiments can be performed by using a ferromagnetic material for the substrate layer, so that an MTJ is formed between the substrate and the particle. Using the same ferromagnetic substrate as a source of spin-polarized electrons allows investigation of spin transfer torque switching behavior.

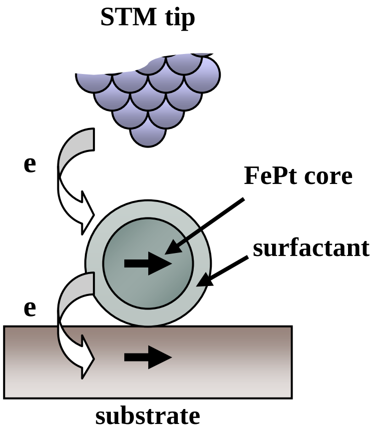

Figure 1.1 – Electrons tunneling through an MTJ structure formed by an STM tip, a magnetic FePt nanoparticle and a magnetic substrate.

In this project the electron transport properties of FePt nanoparticles are studied using STM, aimed at the combination of spin-dependent and single-electron tunneling. The experimental prerequisites for single-electron tunneling are investigated, dealing specifically with sample preparation and practical usage of STM equipment in this context. Chapter 2 of this report will discuss the theoretical background of single-electron tunneling, explicitly applied to the system of nanoparticular samples in a scanning tunneling microscope. Chapter 3 goes into the details of sample preparation, considering the need to anchor FePt nanoparticles to the substrate surface and to isolate those particles from their neighbors. Chapter 4 will move on to review the single-electron tunneling experiment results obtained applying the concepts introduced in the preceding chapters. A concluding discussion will finally be presented in Chapter 5.

2 Single Electron Tunneling

Since charge is quantized to the elementary charge carrier, it may appear at first glance that single electron tunneling (SET) is a rather trivial affair. In practice however a typical conductor allows for transfer of any fraction (or non-integer multiple) of the elementary charge, because the current does not consist of single electrons entering and exiting the material. Conduction instead arises from the net movement of the electron cloud with respect to the ionized nuclei of the material lattice, as illustrated in Figure 2.1. As this movement spans a continuous range, transferred charge also becomes a continuous parameter. Thus current is in fact not quantized.

There are however systems where single electron transport becomes possible. Although one can already recognize the quantized character of conduction across a tunnel junction, net current in such a case may still be continuous due to accumulation of charges at the junction interfaces. If however one introduces a second tunneling barrier in series with the first, single electron tunneling can be observed through the effect known as Coulomb blockade.

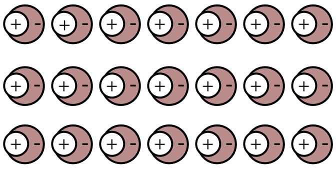

Figure 2.1 – Movement of the electron gas with respect to the lattice ions is not quantized.

This chapter will explain the occurrence of Coulomb blockade in double junction systems and detail the use of scanning tunneling microscopy for SET experiments. Subsequently the experimental investigation of magnetic nanoparticles will be discussed, explaining the use of single electron tunneling to enhance the tunneling magnetoresistance (TMR) and the possible application of spin transfer torque for switching the magnetic orientation of a particle.

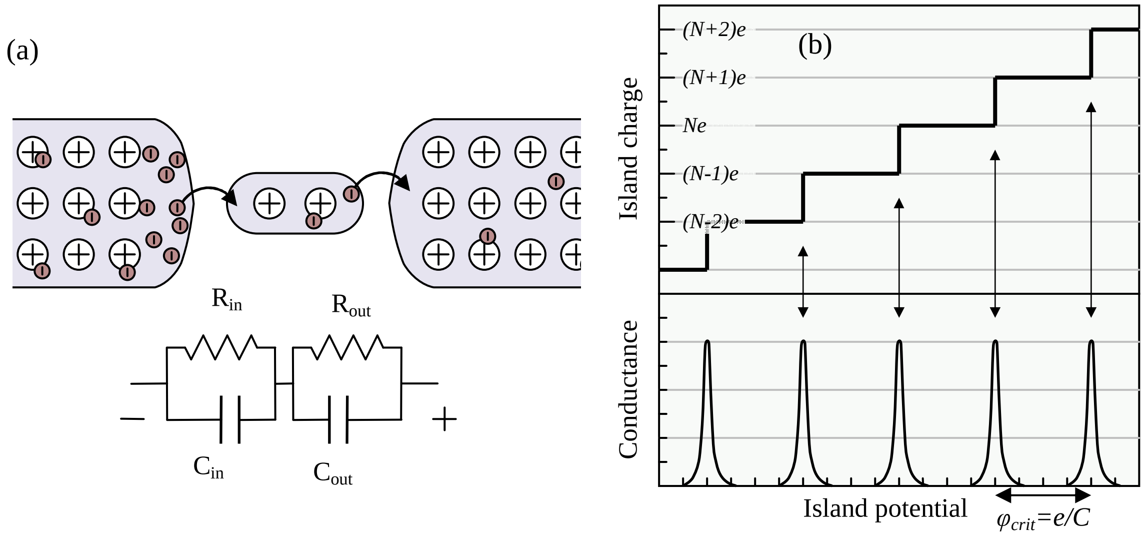

Figure 2.2 – (a) Schematic view of a double tunnel junction enabling single-electron tunneling onto an isolated node. The equivalent electrical schematic consists of capacitive coupling and DC tunneling resistances. (b) SET leads to an integer number of electrons on the island, depending on the node potential [17].

2.1 Coulomb blockade in a double tunnel junction

The origin of Coulomb blockade of a double tunnel junction can be found at the node between the two barriers (see Figure 2.2a). Recognizing that conduction to and from this isolated node can only occur through tunneling of individual electrons, it becomes clear that the node can be charged only by an integer amount of tunneling electrons: $Q = N \cdot e$ where $N \in \mathbb{Z}$. Because of electrostatic repulsion of those charges, a certain amount of energy is required to add an electron to the node, as illustrated in the band diagram of Figure 2.3a.

If we model the isolated node to be capacitively coupled to its surroundings, the total energy associated with that node can be expressed as the sum of the electrostatic charging energy and the potential energy of the node;

$$E(N) = \frac{(N \cdot e)^2}{2C} - \varphi \cdot N \cdot e\,, \tag{2.1}$$

where N is an integer number of electrons with charge e, C is the total capacitance between the node and its surroundings and φ is the electrostatic potential of the node [17].

The critical potential φ_{crit} required for adding one electron can be obtained by solving $E(N+1) = E(N)$, yielding

$$\varphi_{crit} = \frac{e \cdot (2N+1)}{2C}\,. \tag{2.2}$$

For $N=0$ this result yields the threshold potential required for electrons to tunnel into the first available state of the isolated node, corresponding to the first charge plateau in Figure 2.2b;

$$\varphi_{th} = \frac{e}{2C}\,. \tag{2.3}$$

As long as φ is kept between two critical values $\varphi_{crit}(N) \le \varphi < \varphi_{crit}(N+1)$ the charging level of the node will remain constant. This leads to the step-like charge-voltage relationship shown in Figure 2.2b. Consequently, due to the finite residual time of an electron on the island, the tunneling current will also increase step-wise with the voltage (see also Figure 2.3 b and c). For either case the difference in potential between two steps can be computed as

$$\begin{aligned} \varphi_{crit}(N+1) - \varphi_{crit}(N) &= \frac{e(2(N+1)+1)}{2C} - \frac{e(2N+1)}{2C} \\ &= \frac{e}{C}\,. \end{aligned} \tag{2.4}$$

At non-zero temperatures the total charge on the isolated node is not governed solely by the electrostatic potential. Thermal activation will allow electrons to tunnel even if the potential of the island is lower than the critical value. Observing the Coulomb blockade therefore requires the thermal energy to be much lower than the Coulomb charging energy,

$$E_t = k_B \cdot T << E_c = e \cdot \varphi_{crit} = \frac{e^2}{C}\,, \tag{2.5}$$

where k_B is the Boltzmann constant and T the temperature in Kelvin. This shows that the capacitive coupling to the island should be extremely small; with thermal energy being several meV for temperatures below room temperature, the capacitance required is on the order of attofarads.

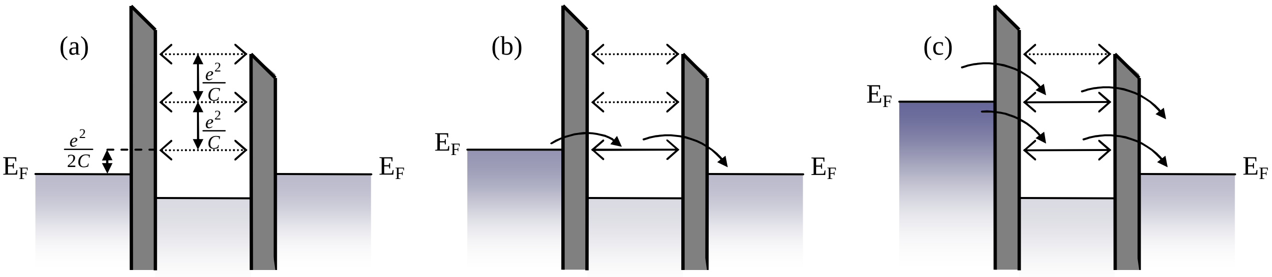

Figure 2.3 – Band diagrams of a quantum dot separated from two metal electrodes by tunnel barriers. (a) Blockade of current due to Coulomb repulsion. (b) Single-electron tunneling when the potential energy reaches the threshold value $e^2/2C$. (c) Double-electron tunneling when the potential is increased by the charging energy e^2/C.

In order to observe Coulomb blockade the electrons must be strongly confined to the isolated node. This means that the tunnel barriers must be sufficiently opaque, or the tunnel resistances sufficiently high. To obtain a measure for the minimum tunnel resistance, we consider the energy/time uncertainty due to the principle of indeterminacy;

$$\delta E \cdot \delta\tau \geq h, \tag{2.6}$$

where h is Planck's constant. Strong confinement of the electrons means that the average time an electron resides on the island must be much larger than the quantum uncertainty of that time, $\tau >> \delta\tau$. Furthermore the uncertainty of the electron energy cannot be larger than the energy potential of the island, $\delta E < e \cdot \varphi$. Inserting these two relationships into Equation (2.6) we obtain

$$\varphi >> \frac{h}{e \cdot \tau}. \tag{2.7}$$

For low potentials only a small number n of surplus electrons can reside on the island at the same time, so the mean occupation time τ limits the total tunneling current I to

$$I \leq \frac{n \cdot e}{\tau}. \tag{2.8}$$

Using Equations (2.6), (2.7) and (2.8), the minimal required tunneling resistance can be expressed as

$$R_t = \frac{\varphi}{I} \geq \frac{\varphi \cdot \tau}{n \cdot e} >> \frac{h}{e^2}. \tag{2.9}$$

The constant $h/e^2 \approx 26$ kΩ is the resistance quantum R_K, and the condition that $R_t >> R_K$ is easily met in the case of tunnel junctions on the order of a nanometer thick.

2.2 The Coulomb staircase

Up until now we have assumed that the island charge level is governed entirely by the tunneling of electrons into the isolated node. However although Equation (2.2) holds for any integer N, the picture of single and double-electron tunneling (and so on) as drawn in Figure 2.3 can only be maintained if the island remains charged. This means we must also consider the tunneling of electrons out of the island into the low-potential electrode.

Figure 2.4 shows two cases that take into account both the tunneling rate into and out of the isolated node (Γ_{in} and Γ_{out}, respectively). If the outbound tunneling rate is very high the island charge will continuously dissipate, leaving even the lowest island states available for tunneling.

This means that beyond the initial threshold voltage (Equation (2.3)), the tunneling current will no longer be blocked (Figure 2.4a).

If on the other hand the outbound tunneling rate is low with respect to the inbound rate, the outbound tunneling becomes a limiting factor and the charge state of the island is maintained. This means that the tunneling current is repeatedly blocked until the voltage potential can overcome the charging level (Figure 2.4b). This leads to the characteristically stepwise current-voltage relationship known as the Coulomb staircase.

Modeling the DC tunneling behavior using only the resistances shown in Figure 2.2a, the inbound and outbound tunneling rates can be described by the inverse of the tunnel resistances R_{in} and R_{out}. With this, the requirement for observing the Coulomb staircase becomes simply $R_{out} >> R_{in}$.

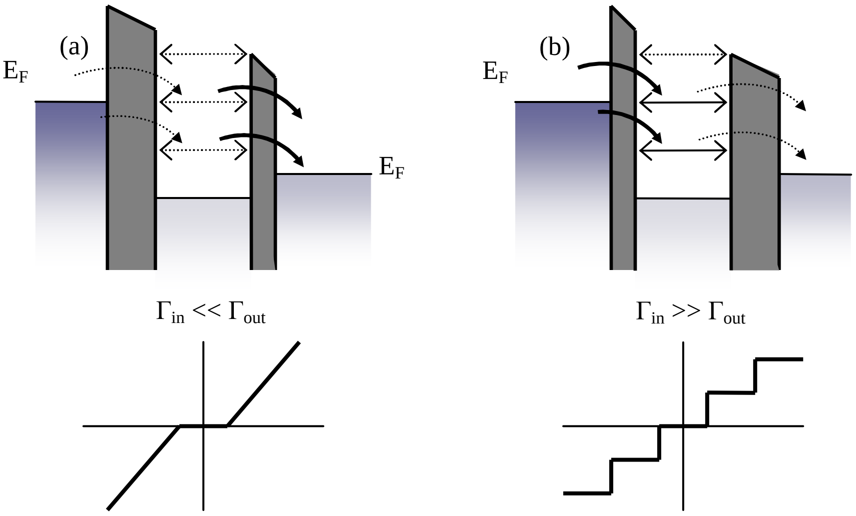

Figure 2.4 – Band diagrams of a quantum dot separated from two metal electrodes by unequal tunnel barriers. (a) Node charging cannot be maintained due to a high outbound tunneling rate. (b) Low outbound rate limits charge dissipation, leading to the Coulomb staircase.

2.3 Junction capacitance

As has become clear from the previous sections, the junction capacitances play a vital role in Coulomb blockade experiments. The extremely low capacitances required preclude the use of thin-film planar tunnel junctions, but isolated nanoislands can be fabricated in a number of ways [11, 17, 18].

In first-order approximation, small islands can be modeled as perfectly isolated spherical conductors, the self-capacitance of which can be computed as follows. Applying Gauss' law to a charged conducting sphere of radius R the electric field outside of the sphere is described as

$$E = \frac{Q}{4\pi \cdot \varepsilon_0 \cdot \varepsilon_r \cdot r^2}, \tag{2.10}$$

with $r > R$ the distance from the center of the sphere. The voltage difference between the sphere (radius R) and a spherical conducting shell surrounding it (radius A) can be computed by taking the radial line integral of the electric field:

$$\Delta V = \frac{Q}{4\pi \cdot \varepsilon_0 \cdot \varepsilon_r} \int_R^A \frac{1}{r^2} dr = \frac{Q}{4\pi \cdot \varepsilon_0 \cdot \varepsilon_r} \left(\frac{1}{R} - \frac{1}{A} \right). \tag{2.11}$$

Taking the limit $A \to \infty$ for a perfectly isolated sphere, we can then calculate the self-capacitance as

$$C = \frac{Q}{\Delta V} = 4\pi \cdot \varepsilon_0 \cdot \varepsilon_r \cdot R. \tag{2.12}$$

In a practical situation a nanoisland is never truly isolated from its surroundings, so to improve this model we can compute the capacitance between a conducting sphere (the island) and a metallic plane (a substrate surface). An expression for this capacitance has been reported to be

$$C = 4\pi \cdot \varepsilon_0 \cdot \varepsilon_r \cdot R \cdot \sinh \alpha \sum_{n=2}^{\infty} \frac{1}{\sinh(n \cdot \alpha)}, \tag{2.13}$$

where $\alpha = \cosh^{-1}(1+\zeta)$, $\zeta = g/R$, g is the particle-substrate gap size and R the radius of the nanoisland [19].

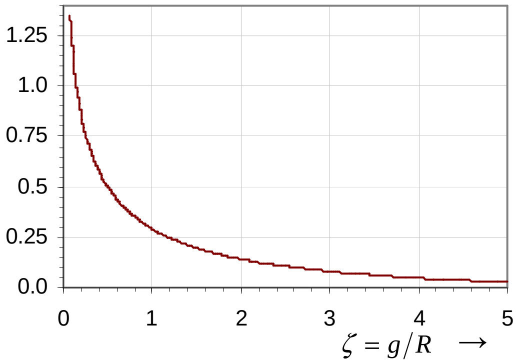

Figure 2.5 – The right-hand part of Equation (2.13) can be interpreted as a 'coupling factor' depending on the ratio of the particle-substrate gap g to the particle radius R.

The prefactor in Equation (2.13) equals the expression for self-capacitance derived above. The other half might thus be considered a factor accounting for the coupling between the island and the substrate. This right-hand part of the equation is plotted in Figure 2.5, showing a monotonous decrease with increasing $\zeta = g/R$. This means that if the island radius R is reduced, both the self-capacitance and the coupling factor will decrease. This agrees with the intuitive notion that in a shrinking system the capacitance should go down. Similarly a decreasing particle-substrate separation g will lead to a larger coupling factor, which agrees with a zero-order image of decreasing separation in a parallel plate capacitor.

2.4 Coulomb blockade experiments using STM

Typical devices for studying Coulomb blockade are fabricated by embedding, or lithographically structuring, conducting nanoislands in thin insulating films [11, 20, 21]. As it is very difficult to fabricate a large number of nanoparticles with identical properties, the single-electron tunneling effects in these devices are averaged out due to distributions in particle size and interparticle spacing. This means that this approach is not suitable for actual single-particle investigations.

A more direct tool for contacting individual particles is the scanning tunneling microscope, a schematic representation of which is shown in Figure 2.6. In essence, the STM consists of a sharp-tipped metal probe (typically either platinum-iridium or tungsten) which is connected to a (piezoelectric) positioning rod. This piezo rod can be used to scan the tip across the X-Y plane and simultaneously regulates the position of the tip in Z-direction. By applying a voltage between the tip and a (conducting) substrate a tunneling current can be measured. A feedback loop is then used to regulate the Z-position of the tip such that this current remains constant at a specific setpoint. As the tip is scanned across a surface, the feedback positioning signal is a measure for the topography.

An STM offers very fine control over tip position, and the setpoint control of the feedback loop allows relatively easy variation of (the ratio between) the tunnel resistances. This makes the STM an effective tool for Coulomb blockade experiments. However, as a tunneling current depends entirely on the amount of free states an electron can tunnel into, the physical quantity actually measured by an STM is the density of states of the target material. It should therefore be noted that a topographical STM image is a derived result, where poorly conducting materials (including nanoparticles in blockade) can adversely affect the topographical accuracy.

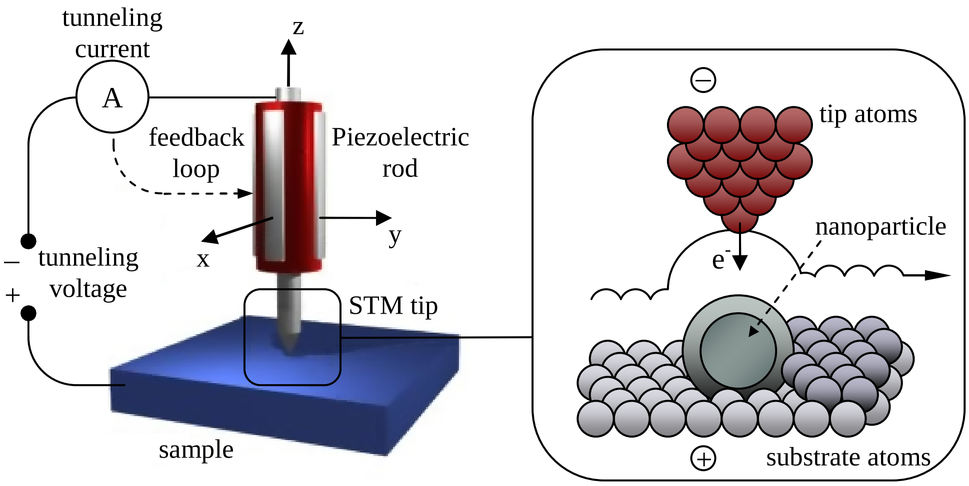

Figure 2.6 –Using a scanning tunneling microscope for single-electron tunneling experiments on a spherical nanoparticle [22]. The piezoelectric rod is controlled by the feedback loop in order to maintain a constant tunneling current between the probe needle and the sample. The isolated particle (not drawn to scale) is capacitively coupled to the substrate and the tip of the STM probe.

Using the STM setup of Figure 2.6 we can give a more specific estimate of the required nanoparticle capacitance. Assuming $E_T < 3.5k_BT$ (typical full width at half maximum of the thermal energy), observing Coulomb blockade at room temperature requires a total capacitance of at most 1.8 aF (Equation (2.5)). For a nanoparticle 4 nm in diameter positioned 1 nm from a substrate plane, using $\varepsilon_r = 2.5$ (typical of alkanethiols, as have been used in this project for nanoparticle immobilization), Equation (2.13) evaluates to a capacitance of 0.87 aF.

This result does however not yet take into account the capacitive coupling between the nanoparticle and the STM tip. If we assume the tip to be terminated by a single atom, the tip-particle system can be approximated by two spheres of different radii. While it is possible to compute the exact capacitance between two conducting spheres [23], a simpler model can be used if we assume the tip radius r_{tip} to be much smaller than the particle radius $r_{particle}$. In that case the tip can be thought to hover over the semi-flat surface of a much larger particle. This allows the application of Equation (2.13), with $R = r_{tip} << r_{particle}$. A smaller radius R leads to a smaller capacitance, so (at comparable separation*)* the tip-particle capacitance should be smaller than the particle-substrate capacitance. The total capacitive coupling between the nanoparticle and the surroundings (substrate and STM tip) can therefore be expected to be no more than twice the particle-substrate capacitance; C_{total} < 1.75aF. This would correspond to a Coulomb charging energy of > 90 meV.

It can be concluded that Coulomb blockade of a 4 nm nanoparticle at room temperature ($E_T \approx 25$ meV) might be observable in an STM. This result is however based on a strongly simplified model, so in practice it may be required to go to lower temperatures in order to decrease the thermal energy. Cooling down the system to below 50 K would increase the maximum allowed capacitive coupling by a factor of 6 or 7, which should make it significantly easier to observe the blockade.

2.5 Nanoparticle magnetoresistance

The FePt nanoparticles investigated in this project are ferromagnetic at low temperatures. The most straightforward aspect of spin-dependent transport is the rise of the magnetoresistance when two magnetic materials are brought into close contact with each other. In the case of a magnetic tunnel junction (MTJ), the density of states at the Fermi level on either side of the junction is spin-polarized and the tunneling current becomes dependent on the relative magnetic orientation of the two ferromagnetic layers (see Figure 2.7).

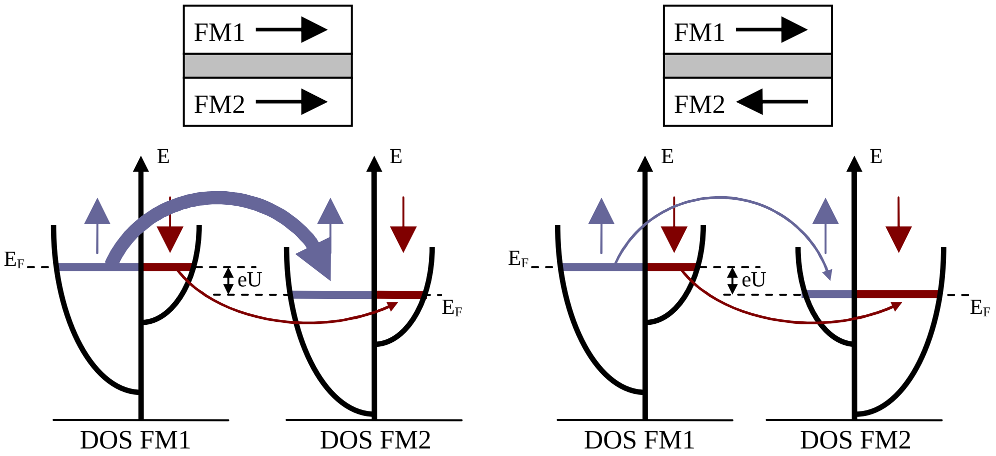

Figure 2.7 – Magnetic tunnel junctions consisting of two ferromagnetic contacts separated by an isolating barrier. A spin-polarized density of states, indicated by the arrows, leads to high tunneling conductance for the parallel orientation (left) and low tunneling conductance for the anti-parallel orientation (right) [24].

In the case of an STM experiment on ferromagnetic nanoparticles, a magnetic substrate layer and some form of tunnel barrier become necessary to form a complete MTJ. As small nanoparticles typically require large magnetic fields to switch magnetization below their Curie temperature, the magnetic substrate should have a low coercivity so as to be able to differentiate between substrate and nanoparticle switching. TMR is defined as the relative resistance change between parallel (P) and anti-parallel (AP) magnetic orientations,

$$TMR = \frac{R_{AP} - R_P}{R_P}, \tag{2.14}$$

so a typical TMR experiment would consist of measuring the tunnel resistance in the parallel state, reversing the magnetic orientation of the substrate layer (anti-parallel state) and measuring the tunnel resistance again.

Bulk ferromagnetic materials generally form multiple domains to minimize the magnetic free energy. As system dimensions decrease however, there comes a point where the domain wall energy is greater than the magnetostatic energy and the magnet forms only a single domain. In the case of magnetic nanoparticles a few nanometers in size, this situation can be readily achieved.

On one hand this means that below the Curie temperature all nanoparticles can be spontaneously magnetized. On the other hand the magnetization orientation of individual nanoparticles will be random, unless the particles are cooled below Curie temperature in the presence of a (strong) external magnetic field (‘field cooling’). In the case of random nanoparticle magnetization the alignment of most particles will be only partially parallel or anti-parallel to the substrate layer, as illustrated in Figure 2.8.

It should be noted that magnetic switching of a single-domain nanoparticle can only occur through direct magnetization rotation and not through domain wall propagation or domain nucleation. Physical rotation of the particle, however, will also effectively rotate the magnetic orientation.

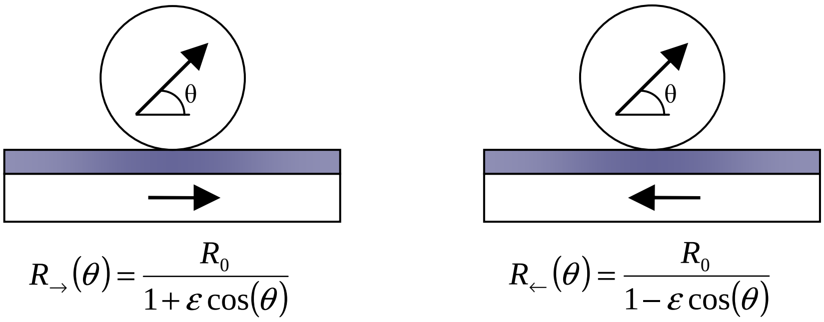

Figure 2.8 – Random magnetization orientation of the nanoparticle will lead to partial misalignment with the substrate layer. In the extreme case of θ=±90° switching the substrate layer has no effect on the tunneling resistance ($R_{\rightarrow} = R_{\leftarrow}$*) and the TMR vanishes.*

Reference [25] derives an expression for the dependence of the tunneling conductance on the angle θ between the magnetization orientations of the two magnetic contacts in an MTJ;

$$G = G_0\left(1+\varepsilon\cos(\theta)\right), \tag{2.15}$$

where G_0 is a base conductance depending on geometric and material properties and the scaling factor ε is a measure for the effective spin polarization in the device. In a perfect system (100% spin polarization) ε would be unity, with the conductance going to zero for a fully anti-parallel orientation.

Defining $R_{\rightarrow}$ ($R_{\leftarrow}$) as the tunneling resistance when the substrate is magnetized to the right (left) in Figure 2.8,

$$R_{\rightarrow}(\theta)=\frac{R_0}{1+\varepsilon\cos(\theta)} \tag{2.16}$$

$$R_{\leftarrow}(\theta)=\frac{R_0}{1+\varepsilon\cos(\theta+\pi)}=\frac{R_0}{1-\varepsilon\cos(\theta)}, \tag{2.17}$$

the TMR dependence on the alignment angle (assuming -90<θ<90) can be computed as

$$TMR(\theta)=\frac{R_{\leftarrow}-R_{\rightarrow}}{R_{\rightarrow}}=\frac{1+\varepsilon\cos(\theta)}{1-\varepsilon\cos(\theta)}-1. \tag{2.18}$$

Plotting Equation (2.18) for ε=0.1 and ε=0.9 (Figure 2.9) illustrates the advantage of using high-ε materials in an MTJ. For very large spin polarization, such as obtainable in half-metals, the TMR can reach much higher values ($TMR(\theta) \rightarrow \infty$ as $\varepsilon \rightarrow 1$). It is also visible that the TMR is highest when the particle is completely aligned (θ=0), and decreases with increasing angle. In the extreme case where the nanoparticle orientation is perpendicular to the substrate the TMR completely vanishes ($TMR\left(\frac{1}{2}\pi\right) = 0$).

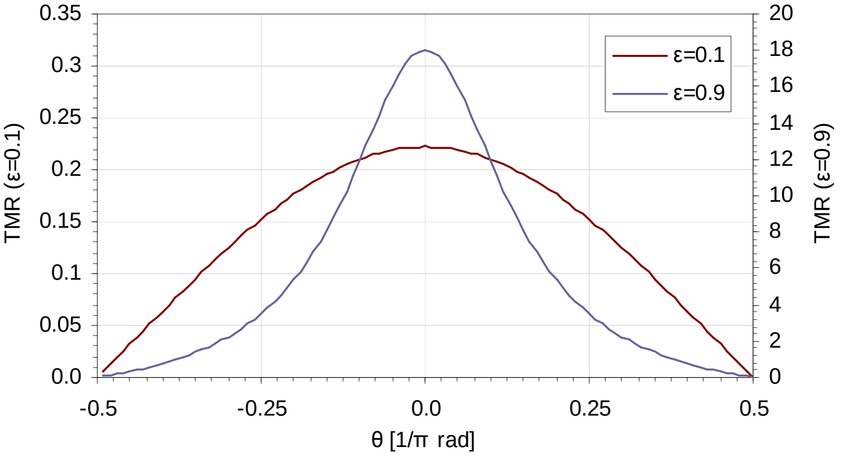

Figure 2.9 – Tunneling magnetoresistance as a function of particle-substrate alignment angle θ *for two values of effective spin polarization factor* ε*. The TMR signal goes to zero as the angle approaches full misalignment (particle magnetization perpendicular to the substrate). A higher* ε *strongly increases the TMR.*

2.6 Combining TMR experiments with SET

Since observing a TMR between a nanoparticle and a magnetic substrate requires electrons to tunnel through the nanoparticle, it can be combined with single electron tunneling as described in Section 2.1. It has been reported that at the Coulomb threshold voltage the TMR signal of a magnetic nanoparticle can be significantly enhanced [12, 13, 14], which is of particular interest when considering data storage applications as an increase in TMR corresponds to an increase in readout signal.

A common explanation of the TMR enhancement is based on the concept of spin-sensitive cotunneling. For a small nanoparticle in strong Coulomb blockade, first-order tunneling becomes very unlikely as electrons do not have enough thermal energy to overcome the Coulomb charge repulsion. This means that cotunneling events, which are higher-order tunneling processes, are the only way to transport electrons through the double barrier system.

Figure 2.10 illustrates an electron tunneling from the STM tip to the substrate through a cotunneling process. Although its thermal energy is classically not high enough to overcome the Coulomb blockade, the Heisenberg uncertainty principle allows the electron to tunnel into what is called a virtual state in the nanoparticle, after which it tunnels out to a state in the low-potential electrode. As long as there is a net energy gain in tunneling across the double tunnel junction, the energy conservation law is not broken on a system-wide scale and current can flow even if first-order tunneling is suppressed [26].

At voltages above the Coulomb blockade threshold cotunneling events can generally be seen as a noise source, turning a sharp staircase into a smoother line. Because of the spin sensitivity of these cotunneling processes however, the relation between parallel and anti-parallel tunneling resistances changes and and the TMR effect can be enhanced [14].

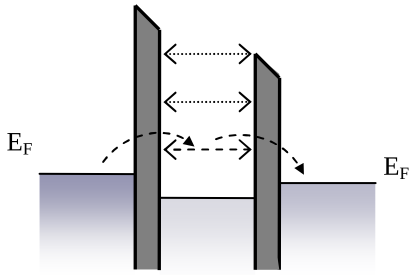

Figure 2.10 – Energy diagram for cotunneling. A virtual state on the island allows an electron to tunnel despite the Coulomb blockade.

In light of possible application of ferromagnetic nanoparticles in memory systems, the investigation of nanoparticle switching behavior is also of great interest in this project. One aspect specifically relevant to data storage applications is the use of spin-transfer torque to switch the magnetization direction of a nanoparticle.

The spin-transfer torque effect was predicted independently by two groups in 1996 [27, 28], who calculated that a spin-polarized current flowing perpendicular to the plane of a metallic multilayer can exert a spin torque on the magnetic moment of a magnetic layer strong enough to reorient the magnetization.

A simplified model explaining this effect is presented in reference [31] ('toy model #1') which regards the magnetic layer as a closed box, interacting with a spin flow through spin-dependent electron reflection and transmission coefficients $r_\uparrow$, $r_\downarrow$ and $t_\uparrow$, $t_\downarrow$. A single-electron state with wavevector $\mathbf{k}$ in the $\hat{\mathbf{x}}$ direction is considered with spin orientation in the $\hat{\mathbf{x}}$ - $\hat{\mathbf{z}}$ plane, at an angle θ with respect to the magnetization vector of the magnetic layer (see Figure 2.11).

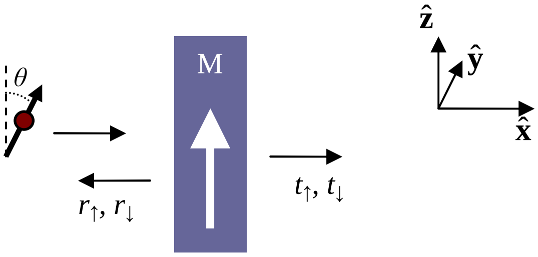

Figure 2.11 – Illustration of ‘toy model #1’, showing an electron incident with a magnetic layer M, spin-polarized at an angle θ with respect to the magnetization vector [31].

For this system the flow of spin density in the $\hat{\mathbf{x}}$ direction for the incident, transmitted and reflected parts of the wavefunction are derived ($\boldsymbol{Q}_{in}$, $\boldsymbol{Q}_{trans}$ and $\boldsymbol{Q}_{refl}$ respectively, not reproduced here), the sum of which is nonzero meaning that spin is not conserved due to the filtering properties of the magnetic layer. Conservation of angular momentum then dictates that the magnetic layer experiences a spin transfer torque $\boldsymbol{N}_{st}$ equal to the net flux of spin current, computed as

$$\begin{aligned}\mathbf{N}_{st} &= A\hat{\mathbf{x}}\cdot\left(\mathbf{Q}_{in}+\mathbf{Q}_{refl}-\mathbf{Q}_{trans}\right)\\ &= \frac{A}{\Omega}\frac{\hbar^2 k}{2m}\sin(\theta)\left[1-\mathrm{Re}\left(t_\uparrow t_\downarrow^* + r_\uparrow r_\downarrow^*\right)\right]\hat{\mathbf{x}}\\ &\quad -\frac{A}{\Omega}\frac{\hbar^2 k}{2m}\sin(\theta)\,\mathrm{Im}\left(t_\uparrow t_\downarrow^* + r_\uparrow r_\downarrow^*\right)\hat{\mathbf{y}}\,,\end{aligned} \tag{2.19}$$

where A is the surface area of the magnetic layer, Ω is a normalization volume, $\hbar$ is the reduced Planck constant and m is the electron mass [31].

If there is no spin filtering ($t_\uparrow = t_\downarrow$ and $r_\uparrow = r_\downarrow$) the above equation evaluates to the general solution (zero torque). Similarly there is no spin transfer torque if the orientation of the incoming spin is collinear with the magnetic layer orientation ($\theta = 0$ or $\theta = \pi$). For any other orientation however the magnetic layer experiences nonzero torque caused by the absorption of spin angular momentum.

Because this torque is perpendicular to the magnetization it is possible to switch the magnetic orientation of the layer if the spin current density is high enough. Reported minimum values of spin-polarized current densities are on the order of 10^7 A/cm^2 [28, 29, 30].

3 Nanoparticle deposition

This research project utilizes $Fe_{0.58}Pt_{0.42}$ nanoparticles several nanometer in diameter, stabilized by oleic acid (bonds with Fe sites) and oleyl amine (bonds with Pt sites), dispersed in hexane. Transmission electron microscopy reveals that approximately 75% of these particles have a size distribution of 3 ± 0.5 nm (see Figure 3.1). As explained in Section 2.4 particles of these diameters could ideally exhibit Coulomb blockade at room temperature.

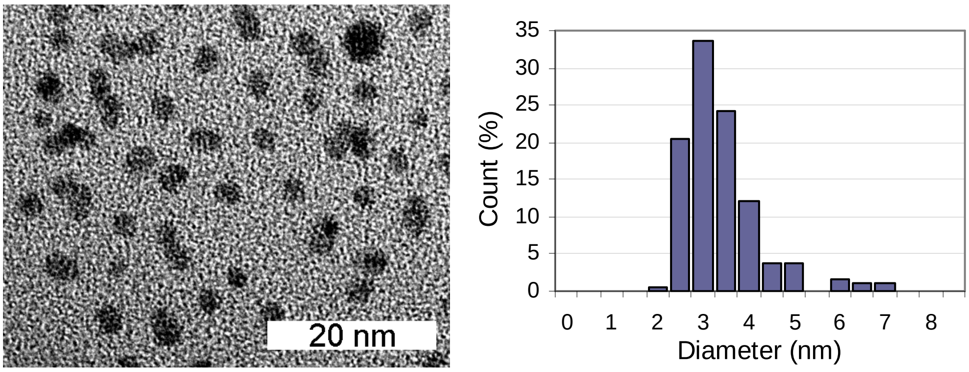

Figure 3.1 – Transmission electron microscope (TEM) image and size histogram of FePt nanoparticles stabilized with oleic acid and oleyl amine molecules.

The magnetic properties of (a layer of) these nanoparticles were measured using a vibrating sample magnetometer (VSM) at room temperature with an in-plane magnetic field, the results of which are shown in Figure 3.2. The curve shows that the particles are superparamagnetic at room temperature and the magnetization saturates at 15 – 20 kOe. However, because of the distribution in particle size and composition, the magnetic reorientation of individual nanoparticles occurs over a range of magnetic field strengths. The magnetization curve shows that at a field of 10-15 kOe most particles should be (almost) fully aligned with the external magnetic field.

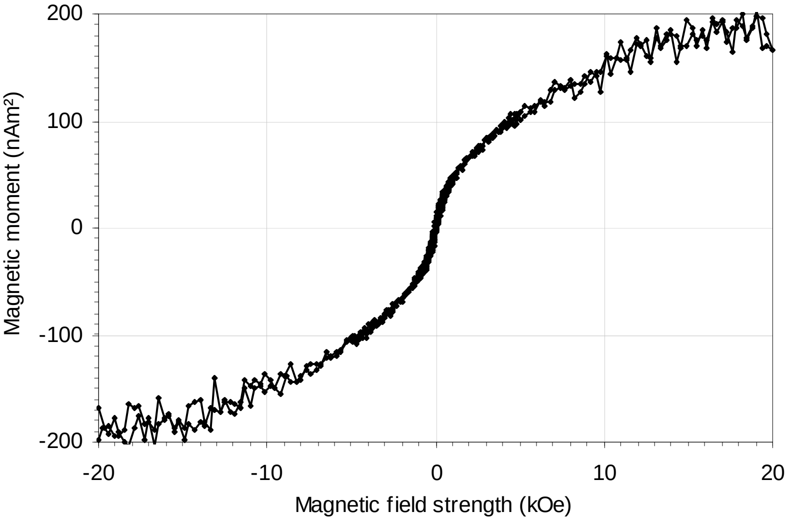

Figure 3.2 – Magnetic behavior of ~3nm FePt nanoparticles at room temperature, measured by VSM. The particles are superparamagnetic and at 10-15 kOe most particles are (mostly) aligned to the external magnetic field.

As will be explained in more detail in the next chapter, the substrates used for sample fabrication in this project are covered either with smooth gold layers or metal oxides. This chapter will discuss the methods used for depositing nanoparticles on those substrates and explain how immobilization of the particles is achieved. AFM and STM imaging results will be presented showing the densities achieved with particle deposition, and some conclusions will be drawn concerning the growth processes.

3.1 Immobilizing nanoparticles on a metal oxide surface

For scanning probe imaging of nanoparticles on flat surfaces it is important to anchor the particles so that the bonding between particle and surface is stronger than eventual attractive or repulsive forces between particle and probe tip. If the attraction to the probe tip is dominant, the particles will likely end up being dragged across the surface or even lifted off the surface completely.

For anchoring particles on metal oxide substrates the procedure described in reference [32] was followed, which consists of depositing a thin film of poly(ethyleneimine) (PEI) as an adhesion layer. PEI is a branched polymer with many NH_2 terminations, which can bond to Pt [33]. When an FePt nanoparticle arrives at the polymer surface it can therefore bond to the PEI through ligand exchange, whereby an amine group in the PEI takes the place of an oleyl amine surfactant molecule on the particle.

To prepare a substrate for deposition of a PEI layer, it is first ultrasonically cleaned in acetone and isopropyl alcohol (10 minutes each at room temperature) and treated with oxygen plasma to activate the surface (2 minutes at 0.25 mbar pressure, 18% O_2 flow and 300 W power). It is then submerged for 5 minutes in a 20 mg/ml solution of PEI in chloroform, after which the surface is rinsed with ethanol. Previous AFM measurements have shown this process to result in a PEI layer thickness of approximately 3 nm [32].

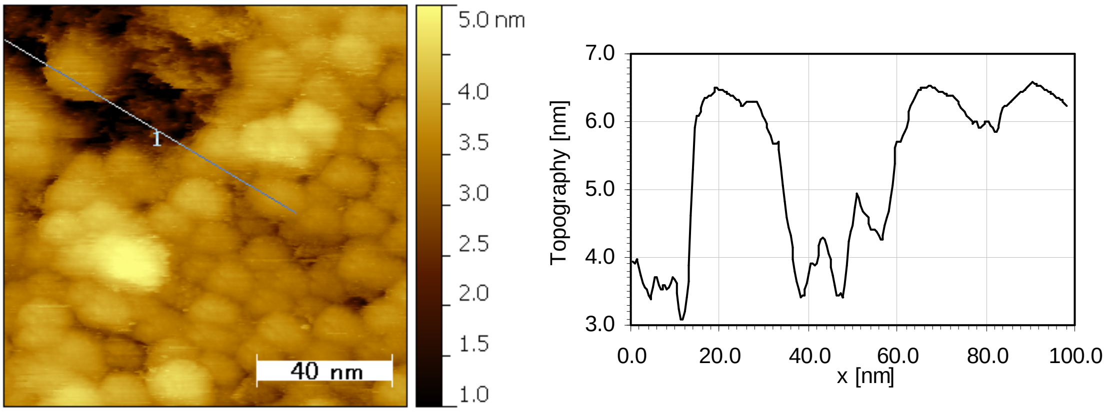

Figure 3.3 – STM topography scan of a nanoparticle monolayer with a height profiles taken along the marked path (I = 0.5 nA, V = 2.75 V), showing relatively dense packing with some open sites.

The performance of PEI was verified by growing a self-assembled monolayer (SAM) of nanoparticles on a Co/Al_2O_3 substrate, as described in aforementioned reference. After PEI deposition the substrate is submerged for 10 minutes in a 10 mg/ml nanoparticle dispersion in hexane. It is then washed in hexane twice and subsequently dried in a flow of nitrogen.

An STM topography scan of the resulting monolayer is displayed in Figure 3.3, showing a semi-continuous layer of nanoparticles with some particles apparently deposited as a secondary layer. It is clear that there are still gaps in the layer. It has been suggested that packing density can be improved with a longer deposition time [32], which suggests that these holes can be filled by prolonged submergence of the substrate in the nanoparticle dispersion. Due to tip-sample convolution the particles appear larger than the aforementioned 3-4 nm, but the height profile shows that the layer thickness is very well matched to this value. The above results were reproducible across several scans, showing that the PEI polymer effectively immobilized the nanoparticles

A second performance parameter for the anchoring layer is the surface roughness. Figure 3.4 shows AFM topography images of a Si/SiO_2/Co(10nm)/Al_2O_3(3nm) surface with and without a thin PEI layer deposited. The scans show equivalent roughness profiles (2 nm peak-peak), indicating that the PEI forms a very smooth layer that follows the shape of the substrate. Low roughness is an important requirement for further STM measurements, as it can become difficult to differentiate between a surface grain and a nanoparticle if the surface roughness becomes comparable to the particle size.

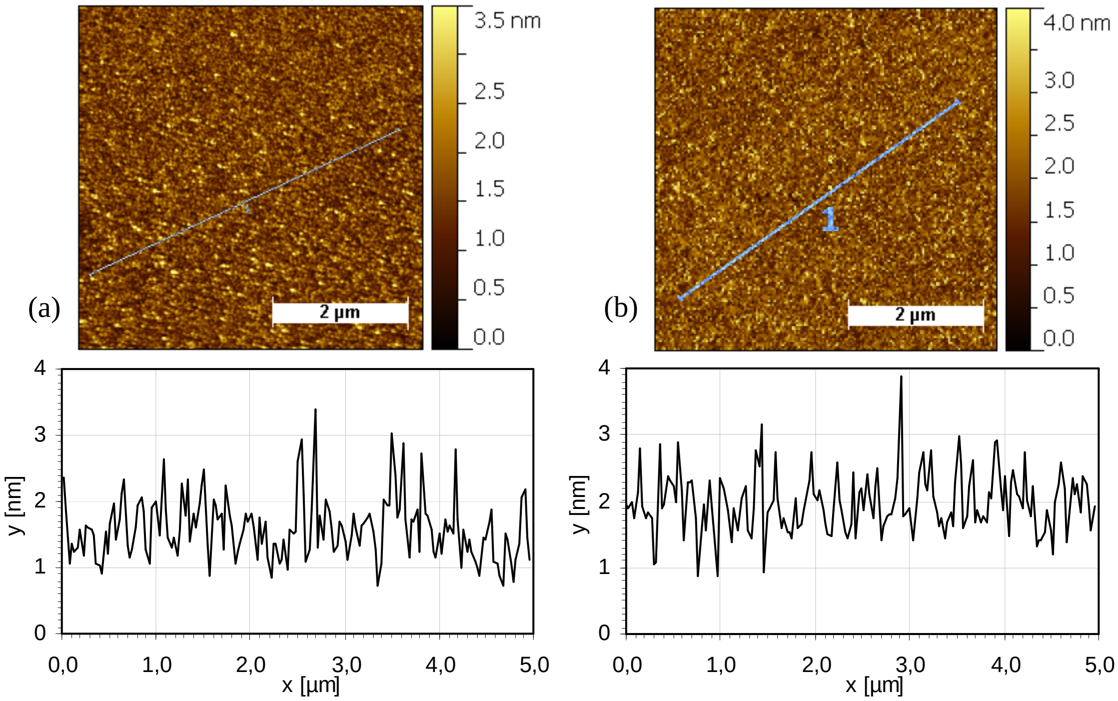

Figure 3.4 – AFM topography scans of an empty Al_2O_3 surface (a) and a ~3 nm PEI layer on an identical Al_2O_3 surface (b), with height profiles measured along the marked paths. The identical roughness properties show that the thin PEI layer conforms to the underlying substrate.

The smoothness of the PEI was however not constant across all experiments, as a later deposition run revealed the formation of triangular protrusions, shown in Figure 3.5. The dimensions of these hillocks differed somewhat between the four samples in this batch. The sample shown on the left shows hillocks approximately 5 nm in height spaced 1 µm apart, while the formations in the right-hand image are about 8 nm in height and 2.5 µm apart. The width in both cases is approximately 0.5 µm. The scans of Figure 3.5 were made after deposition of (low-concentration) FePt nanoparticles, so there is some particulate matter visible in between the hillocks. Ignoring these details, the background roughness appears to be the same as that of the empty PEI layer shown in Figure 3.4b.

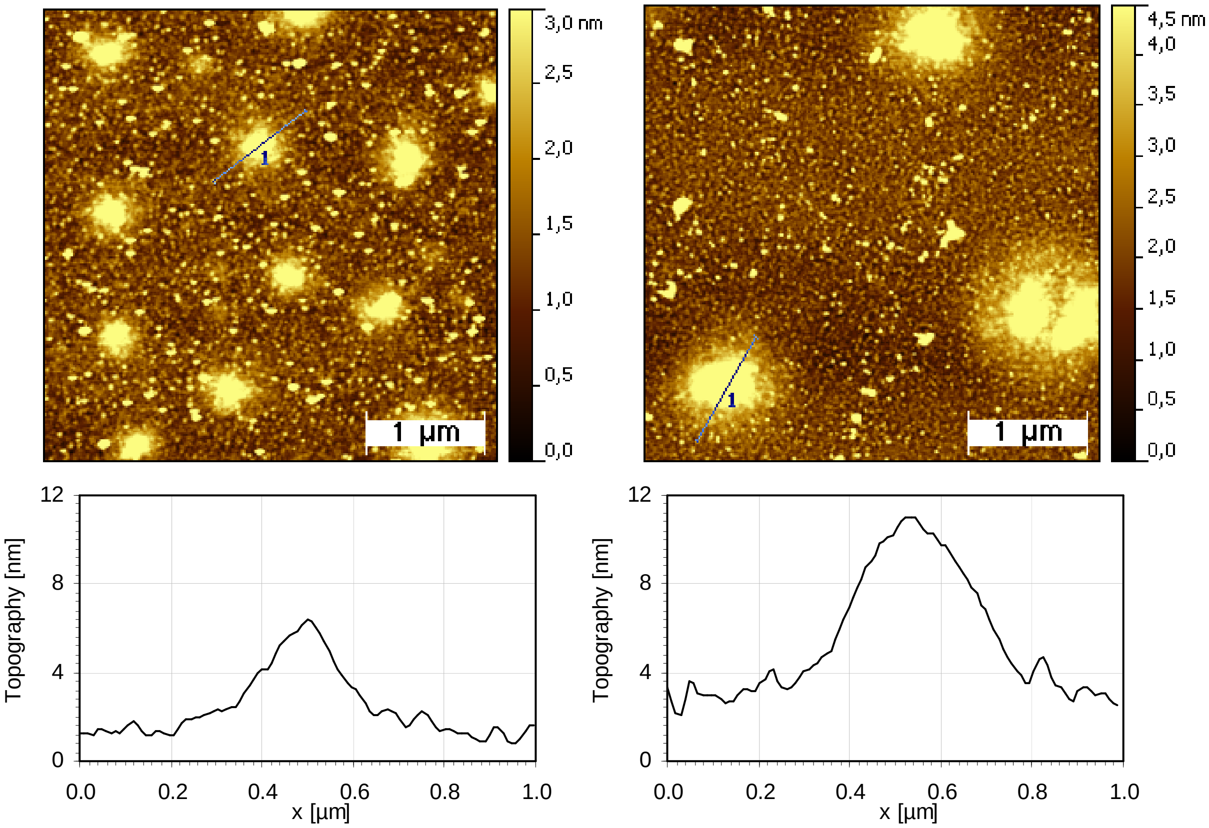

Figure 3.5 – AFM topography scans and cross-sectional height profiles of hillock formations on two samples of PEI on Al_2O_3, measured after nanoparticle deposition. The smooth, wide shape suggests the hillocks are part of the PEI layer, rather than agglomerations of nanoparticles.

The cause of this hillock growth was not clear, but their height being larger than the intended PEI layer thickness of 3 nm suggests that the layer thickness may not be as expected. It was considered that these hillocks are not formed during PEI deposition at all, but are in fact agglomerations of nanoparticles. The smoothness of the wide cross-sectional profile seems to preclude this however, as the particle diameter of 3 nm is already half of the hillock height and thus should lead to more step-like shapes.

3.2 Immobilizing nanoparticles on a gold surface

As will be demonstrated in detail in the following chapter, STM imaging and spectroscopy measurements on substrates with a PEI layer was found to not be trivial due to the relatively thick tunnel barrier between nanoparticles and substrate. For this reason a thinner anchoring layer was selected for gold substrates, based on alkanedithiol molecules. In organic chemistry it is common practice to use alkanethiols to form self-assembled monolayers on noble metal surfaces, and the use of dithiol molecules as an anchor between a gold surface and a noble metal nanoparticle has been reported for STM-based single-electron tunneling experiments in literature [34, 35].

Dithiols being SH-terminated on both ends, the formation of a self-assembled monolayer can be disturbed by dithiol molecules bonding to the substrate with both thiol groups, forming a

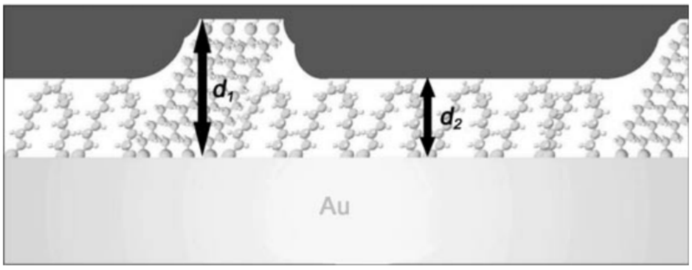

Figure 3.6 – Illustration of a self-assembled monolayer of alkanedithiol molecules on gold, forming both standing-up phase and looping phase grains [37].

back-looping or lying-down phase instead of the required standing-up phase (see Figure 3.6). It has been reported that occurrence of the looping phase increases with increasing chain length [36], and SAM junction tunneling current increasing for molecules longer than 1,14-tetradecanedithiol has been attributed to this effect [37]. This suggests a maximum allowed chain length for SAM growth of mostly standing-up phase dithiols. Kinetic studies of alkanethiol adsorption onto gold(111) surfaces have however shown that the initial growth rate increases with concentration [38], which means that in highly concentrated solutions there will be less free sites for a molecule to loop back to after initial adsorption. The quoted reports show that a dithiol concentration on the order of millimolars leads to fast initial growth and a preferred standing-up phase of SAM growth up to at least 16 carbon atoms long [37, 38].

The formation of the standing-up phase is commonly attributed to the Van der Waals interaction between two adjacent molecules [39]. This can be thought to give a lower boundary on the dithiol chain length, as for very short alkyl chains the Van der Waals energy gained in the standing-up phase may not be enough to overcome the binding energy of the second thiol group. Despite this, highly packed standing-up dithiol SAMs grown by simple immersion of a gold surface in a dithiol solution have been reported with alkyl chains as short as 4 carbon atoms [40].

It should be noted that for this project an entirely standing-up phased SAM is not specifically required, as the goal is not to create a large-scale tunnel junction. If the majority of molecules is standing up, still having one thiol group available for bonding, anchoring of nanoparticles should not be problematic.

The process followed for fabrication of a dithiol SAM on gold is based on the large number of publications on this topic [35, 37, 41-44]. The molecule selected for the anchoring SAM is 1,9-nonanedithiol ($HS-(CH_2)_9-SH$, 'C9'), which is well below the maximum chain length discussed above. Assuming a molecule tilt angle of 30 degrees from the gold surface normal, a nonanedithiol SAM should be approximately 1.1 nm thick [37, 42].

The C9 molecule is dissolved in absolute ethanol at a 3mM concentration. Using ethanol as a solvent is a common choice because of its low toxicity and its availability in high purity at low costs. Also it has a low tendency to be incorporated into the monolayer [38]. The concentration of 3 mM should be sufficient to obtain a mostly standing-up phase SAM, as explained above. After cleaning procedures the gold substrates are submerged in the C9 solution and stored in an argon atmosphere for 17 hours. Then the samples are rinsed with ethanol in order to remove physisorbed layers and molecules from the surface, and the substrate is blown dry with pure nitrogen gas.

Following the SAM formation, the samples are immediately processed for nanoparticle deposition (discussed in the following section) and loaded into the ultra-high vacuum chamber of the STM.

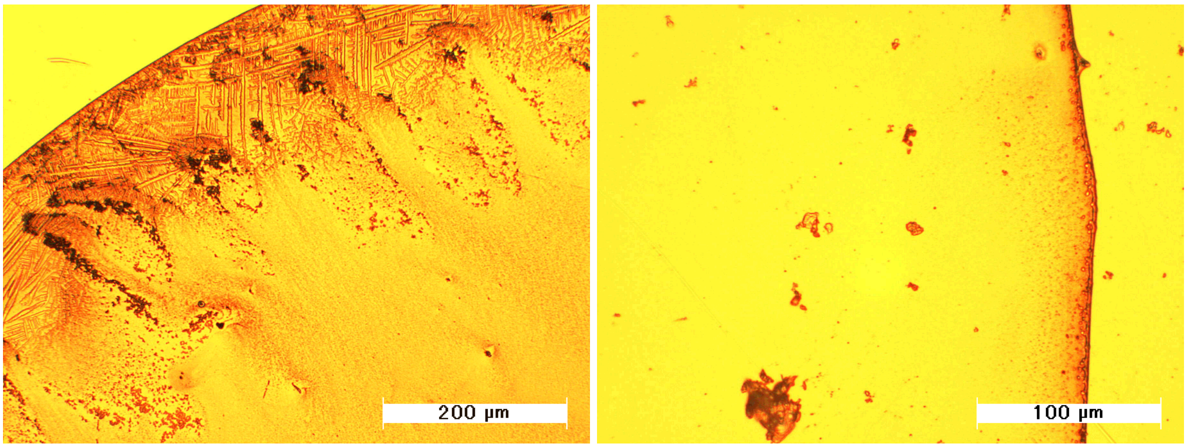

Figure 3.7 – Optical microscopy images of 40 nm gold nanoparticles drop-cast on a gold surface from a saline dispersion. The salt crystals (left) were easily removed by gently washing the sample in water, revealing gradually decreasing particle densities on the surface (right).

3.3 Isolating nanoparticles on a surface

In order to see a clear Coulomb blockade in STM *I-V* spectroscopy it is important to isolate particles from their surroundings as much as possible. Instead of a densely packed monolayer it is therefore preferable to deposit isolated, unclustered nanoparticles. The application of drop casting to obtain this particle isolation has been investigated by casting 5 µl buffered (saline) dispersion of $9{\cdot}10^{10}$ ppml 40nm Au nanoparticles on an empty, sputtered gold surface, chosen because the large diameter renders these particles easily distinguishable in STM topographic imaging. Optical microscopy images of the resulting surface are shown in Figure 3.7. The deposited salt crystals were easily removed by carefully washing the sample in water, leaving large amounts of (agglomerations of) particles on the surface.

The decreasing particle density towards the empty areas suggests that in these regions single isolated particles may be found, which is verified by STM imaging as shown in Figure 3.8. Spherical particles approximately 40 nm in diameter are visible. The granular structure of the gold layer is faintly visible as smooth shapes in the background, so the low-profile island growth across the surface is thought to be salt residue from the solution.

This result suggests that drop casting, while applicable, introduces the risk of polluting the surface with contaminants from the solution. A test with drop casting of FePt nanoparticles from hexane dispersion showed considerable contamination even after washing, so this method was not pursued further.

A second method for achieving particle isolation is modifying the monolayer deposition process. By decreasing the particle concentration of the dispersion it is possible to reduce the particle-surface reaction rate. Similarly the submergence time of the sample can be shortened in order to limit the substrate’s exposure.

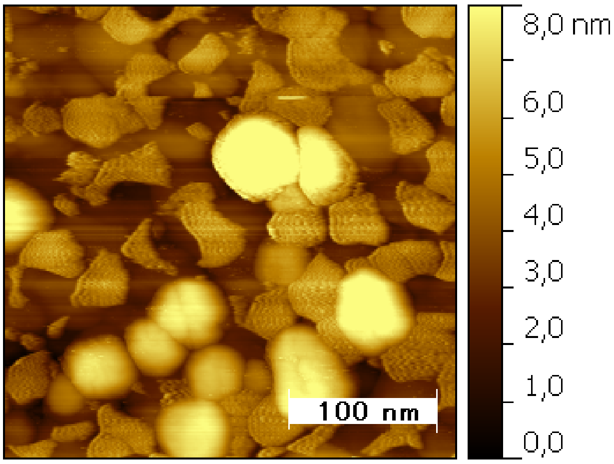

Figure 3.8 – STM microscopy image of 40 nm gold nanoparticles drop-cast on gold (I = 0.4 nA, V = 0.4 V, room temperature).

As described at the beginning of this chapter the deposition of an FePt nanoparticle monolayer uses a 10 mg/ml dispersion of nanoparticles in hexane, in which the sample is submerged for 10 minutes. After decreasing the submergence time to 120, 60 and 23 seconds the resulting particle densities were found to be considerably lower, as is visible when comparing the AFM results of the 23 seconds sample with those of an FePt monolayer (Figure 3.9 a and b, respectively). Despite the lower particle density the cross-sectional analysis illustrates that the visible details are most probably agglomerations of particles, meaning that true particle isolation is not yet achieved.

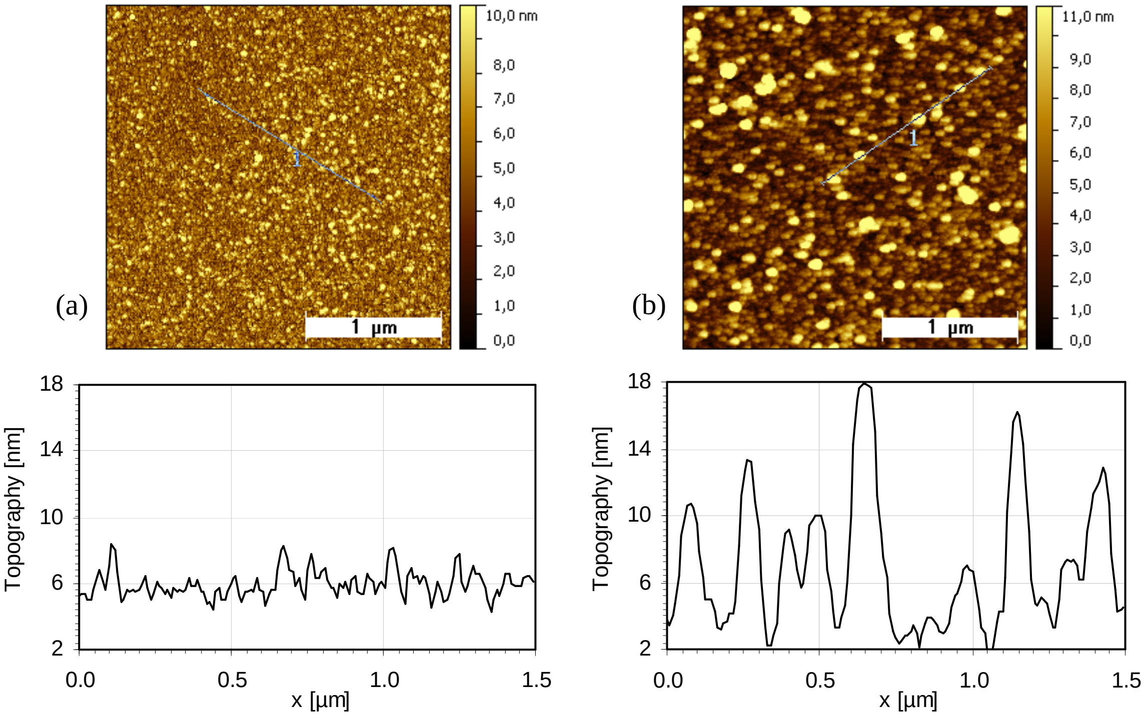

Figure 3.9 – AFM topography scans of FePt nanoparticles deposited on a PEI polymer layer from a 10 mg/ml nanoparticle dispersion, with height profiles taken along the marked paths. (a) Densely packed monolayer, grown by 10 minute submergence. (b) Lower density layer, 23 seconds submergence. Isolated features are visible on this sample, despite an apparent decrease in resolution caused by tip imaging. Large topographical amplitude suggests however that features are agglomerations rather than single particles.

To further improve on these results the nanoparticle dispersion was diluted to 1 mg/ml and samples were submerged for 5, 10 and 20 seconds, the results of which are shown in Figure 3.10. The 5 seconds deposition produces a particle distribution similar to that of the 23 seconds 10 mg/ml sample, while the topography is reduced to 5-6 nm which lies in the range of single particle dimensions.

The reproducibility of this result is however called into question by the longer submergence times, which reveal very different outcomes. Figure 3.10b (10 seconds submergence) shows a very loosely packed but already nearly closed monolayer forming on the surface, with some large agglomerations of particulate matter randomly deposited on top. The openings in the layer reveal that the layer is approximately 3 nm thick, or one monolayer of nanoparticles. Comparing this to the 20 seconds sample (Figure 3.10c) it can be seen that the monolayer packing density increases with submergence time. Interestingly the openings in the layer are much larger in the latter case, which might indicate movement of particles along the surface as the layer self-arranges in a denser packing phase.

It is also quite obvious that the layer openings are formed in a circular pattern, with some particle agglomeration occurring at the edges. Although this pattern suggests some magnetic interaction between the monodomain nanoparticles, their superparamagnetic behavior at room temperature would seem to preclude this: Using an anisotropy constant Ka on the order of 10^5 J/m^3[45] and an attempt period τ_0 of 10^{-9} s [46], the Néel relaxation time at room temperature for a 4 nm FePt nanoparticle can be computed as $\tau_N = \tau_0 \exp\left(K_a V / k_B T\right) \approx 10^{-9}$ s, where V is the nanoparticle volume, k_B is the Boltzmann constant and T the temperature in Kelvin. This extremely short relaxation time should render any magnetic interactions irrelevant on the timescales involved in particles arranging themselves on a surface.

The circular patterning may instead be a result of the sample drying process (nitrogen flow) which could cause the particles to clump together as the solvent film is evaporating. The somewhat circular clustering of nanoparticles around the PEI hillocks shown in Figure 3.5b could be seen to support this, as it is probable that the hexane solvent starts evaporating at the hillocks causing the particles to flow down the slope towards the valleys.

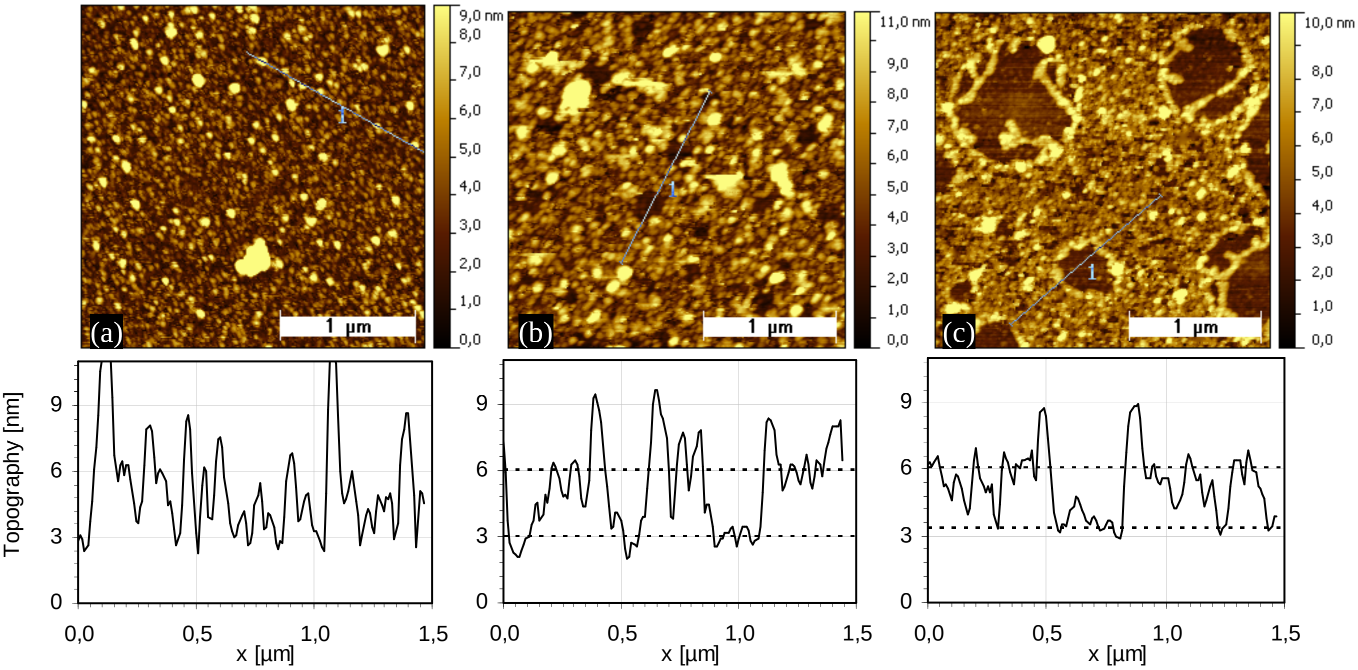

Figure 3.10 – AFM topography scans of FePt nanoparticles deposited on a PEI polymer layer from a 1 mg/ml nanoparticle dispersion, with height profiles taken along the marked paths. (a) Isolated features in the single-particle range (5-6 nm), 5 seconds submergence time. (b) Very loosely packed monolayer of nanoparticles showing some gaps and second-layer precipitates, 10 seconds submergence. (c) Denser monolayer of particles with large, circular gaps and agglomerations along the edges, 20 seconds submergence.

The above results illustrate the very high sensitivity of the growth process to the submergence time. It appears that the self-assembly process is in the first few seconds governed by high-speed adsorption of large amounts of particles which quickly cover the entire service, after which growth switches to an ordering process which increases the packing density.

To obtain a more controllable deposition, the nanoparticle dispersion was diluted to 50 µg/ml to further slow down the nanoparticle deposition kinetics. Figure 3.11 shows the result of 300 second submergence using this concentration, revealing 3-5 nm features that strongly suggest single particle deposition. This notion is enforced by a significant decrease in the

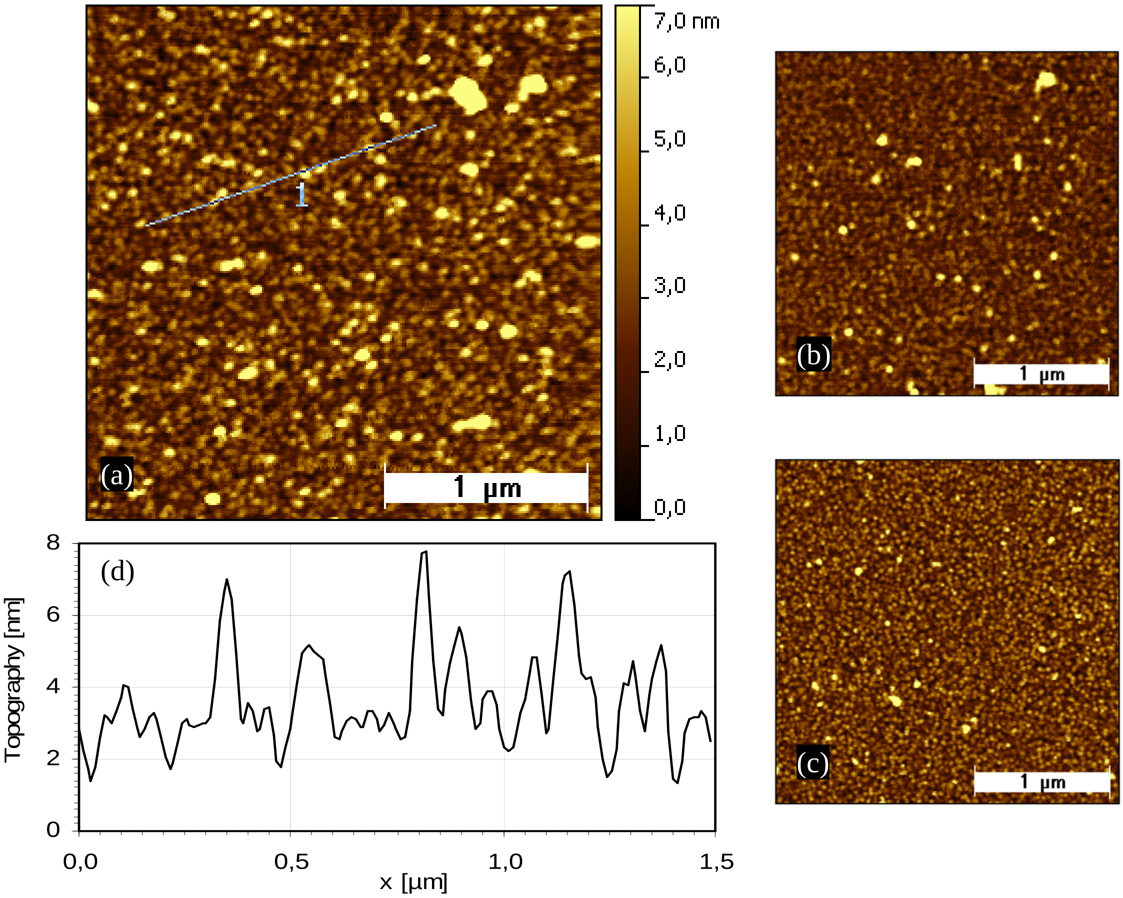

Figure 3.11 – AFM topography scans of FePt nanoparticles deposited on a PEI polymer layer from a 50 μg/ml nanoparticle dispersion, with (a) 300 seconds, (b) 60 seconds and (c) 15 seconds submergence. The height profile (d) shows isolated features between 2 and 6 nm, which is evidence for single particle deposition.

number of agglomerations compared to previous results. A further decrease in particle count is also possible, as illustrated by the 60 and 15 seconds submergence samples (Figure 3.11 b and c, respectively).

This shows that at 50 μg/ml the dispersion concentration is low enough to prevent immediate large-scale adsorption, limiting the deposition process to the speed of nanoparticle diffusion to the substrate surface.

3.4 Anchoring layer performance

The performance of the two anchoring methods described in the previous sections can primarily be measured against their ability to keep isolated FePt nanoparticles immobile during STM topography scanning. Two room-temperature scans of the C9 dithiol system are shown in Figure 3.12. These scans were taken at very low setpoint current in order to increase tip-sample separation, which prevents damage to the dithiol SAM during imaging. The bias voltage was also kept relatively low, partially for protection of the SAM, but also to prevent the PtIr tip from attracting stray dithiol molecules, which would attach themselves to the Pt material and reduce tip quality.

The spotted pattern on the surface is typical for (di)thiol monolayers on gold and has been identified as monatomic steps in the gold substrate, rather than imperfections in the dithiol SAM. The formation of these single-step holes in the gold layer is thought to be caused by an etching effect inherent to the molecular self-assembly processes of thiol adsorption [47-50]. When taking the cross-sectional profile along one such depression (Figure 3.12b, profile 1), the depth indeed equals one Au atomic step (d ≈ 0.25 nm).

Nanoparticles are visible in both scans of Figure 3.12. In the case of subfigure b the particle remained stationary during multiple successive scans, showing that it was firmly attached to the dithiol SAM. As is visible in Figure 3.12a however, other nanoparticles were not as well anchored and were dragged across the surface by the STM tip.

It is interesting to note that the height profile of the stationary particle is only about 0.4 nm, whereas the measured height of the moving particle amounts to more than 1.5 nm. This, together with the fact that the expected particle diameter is around 3 nm, suggests that the anchored particle is in fact embedded in the dithiol layer. When a particle is partially buried in the monolayer, for example at one of the dithiol SAM depression sites, it strongly increases the chance of multiple thiol molecules being adsorbed on the nanoparticle surface and the anchoring becomes much stronger. This could however mean that strongly anchored particles are closer to the gold substrate than the SAM thickness of the C9 dithiol SAM would suggest.

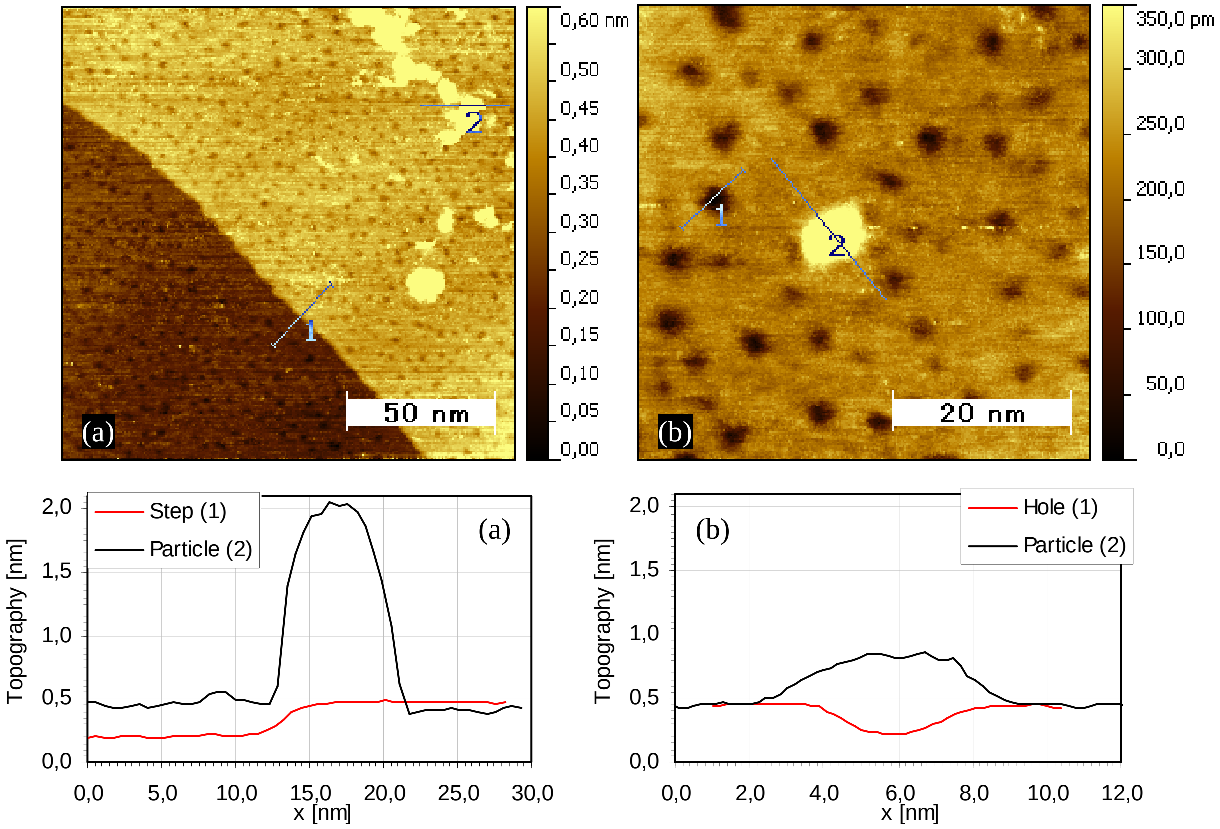

Figure 3.12 – STM topography scans and height profiles of nanoparticles on a C9 dithiol monolayer on gold (V = 0.1 V, I = 50 pA). (a) Monatomic step of Au with a nanoparticle dragged across the surface by the STM tip. The cross-sectional profile measures approximately 1.5 nm in height. (b) Close-up of a strongly anchored nanoparticle, measuring only about 0.4 nm. Both scans show the typical SAM 'holes', which are the same height as one atomic step.

Repeating the experiment at low temperature led to approximately the same results. The topography scans in Figure 3.13 were performed at $T \approx 40$ K and show a strongly anchored nanoparticle, with a measured height of about 0.8 nm, as well as a loose nanoparticle being pushed away by the STM tip, measured at about 0.9 nm. The low temperature appeared to have no influence on the particle immobilization, as nanoparticles could be seen moving across the surface in about half of all topography scans, both at low and room temperature. Anchored nanoparticles, although resolved less commonly than mobile ones, were also found equally often in both experiments.

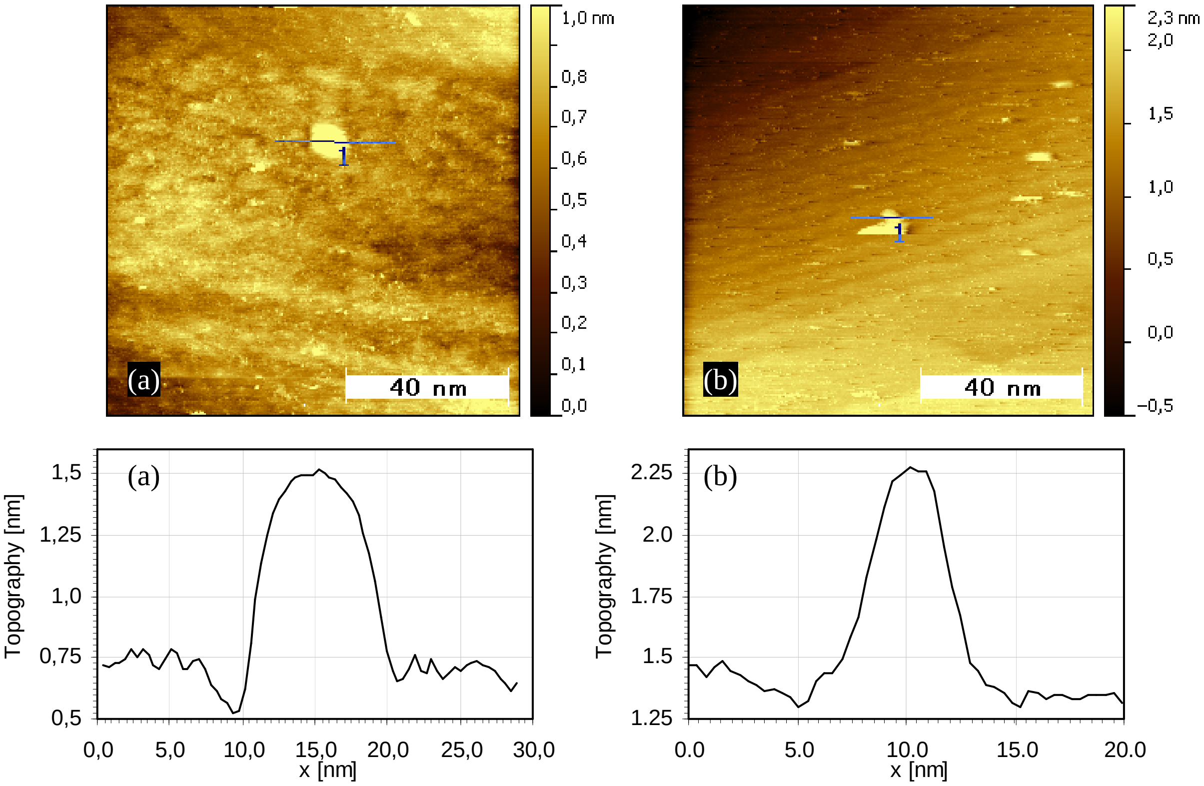

Figure 3.13 – Low-temperature STM topography scans (I = 50 pA, V = 0.5 V, T ≈ 40 K) and height profiles of (a) fixed and (b) mobile nanoparticles on a C9 dithiol SAM.

In the case of Figure 3.13a, some barely visible details can be discerned that may be the depressions in the gold layer described above, but overall it is clear that these scan results are not as detailed as the ones shown in Figure 3.12. Interestingly this problem occurred for all scans at cryogenic temperatures, even when measured at slightly higher voltages to compensate for lower electron energies. As the piezoelectric positioning system of the STM tip should become more stable at lower temperatures, the increased noise and low resolution in low-temperature scans is probably caused by low tip quality or stronger tip-sample interaction.

This effect may be explained by the higher tunneling resistance one can expect at lower temperatures. When cooling down the system any thermally activated hopping conduction, for example through defect states present at the interface or in the SAM, is suppressed. This would force the feedback loop to approach the tip closer to the surface, increasing its interaction with the surface. It is also possible that pollutants such as organic molecules or small nanoparticles are more easily adsorbed onto the STM tip at lower temperature (gettering effect). Such pollutants can introduce secondary conduction paths and greatly reduce scan resolution.

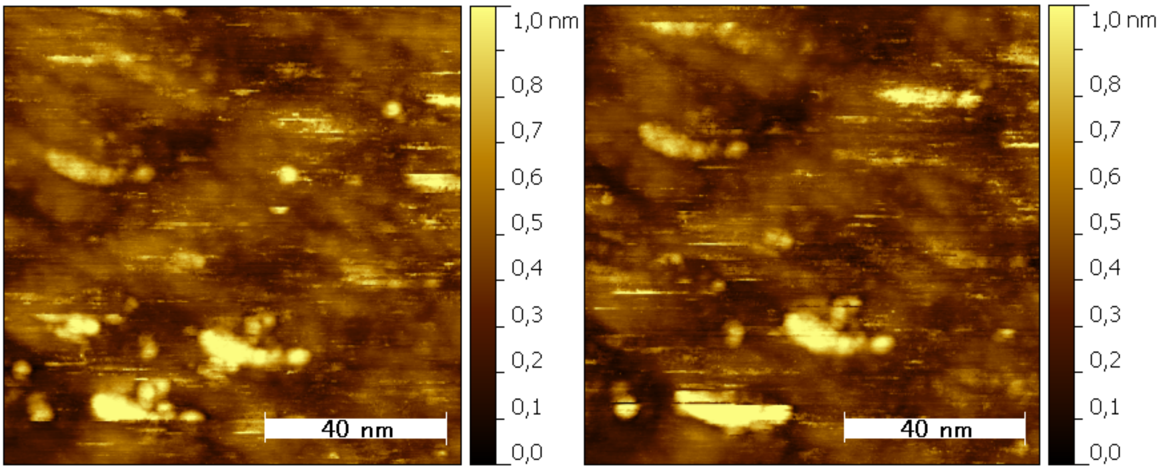

Figure 3.14 – Two sequential STM topography scans showing poor nanoparticle anchoring on an LSMO/PEI surface (I = 50 pA, V = 1 V, room temperature).

Particle anchoring on the PEI polymer layer was investigated on a $La_{0.7}Sr_{0.3}MnO_3$ (LSMO) conducting oxide sample, the fabrication of which will be discussed in more detail in the following chapter. Figure 3.14 shows two successive room-temperature scans of the same area, imaged at a current setpoint of 50 pA and a voltage bias of 1V in order to maintain a large tip-sample separation.

Some nanoparticle can be seen to move during the scan (disappearing either during scanning or in between the two scans), whereas specifically agglomerations of particles remain, for the most part, stationary. Topographic height of both moving and fixed nanoparticles measure approximately 0.7 nm. Isolated nanoparticles with strong substrate anchoring were not readily found on PEI samples, meaning the polymer is much less suited for single particle anchoring than for particle monolayers (Figure 3.3).

This difference means that the attractive and/or repulsive forces of the STM tip, while not sufficient to overcome the anchoring of particles packed in a monolayer, is strong enough to move particles with a larger degree of freedom. This suggests an interaction between the nanoparticles that help the physical stabilization on a surface.

The blurriness of the results above reveals that the quality of the STM tip is quite low. This is probably caused by tip-sample interactions, occurring despite the use of low current and high voltage. Measurement results at $T \approx 40$ K (not shown here) were comparable to those at room temperature, aside from an increase in tip degradation. This issue will be discussed in more detail in the following chapter.

4 Experiments

Having established in the previous chapter a reliable method to deposit isolated nanoparticles on surfaces and immobilize them to some degree, this chapter will detail the STM-based single-electron tunneling and magnetoresistive experiments. The device structures for these experiments will be discussed in detail, and Coulomb blockade in FePt nanoparticles will be demonstrated.

4.1 Sample preparation

In order to facilitate magnetoresistance measurements at a later stage, the first experiments were carried out on samples with a ferromagnetic layer with a tunnel barrier on top. Using a Metal-600 MBE ultrahigh vacuum electron beam evaporator by DCA Instruments, a ~10 nm thin film of cobalt was grown on Si/SiO_2 substrates. This cobalt layer serves as the bottom contact electrode and can form a magnetic tunnel junction (MTJ) together with the magnetic nanoparticles. To prevent atmospheric oxidation, the cobalt is capped with a 2.5 nm aluminum film which is subsequently plasma oxidized to form a ~3 nm aluminum oxide layer. Following the methods described in Chapter 3, the surfaces of these samples are covered with a PEI layer and FePt nanoparticles are deposited.

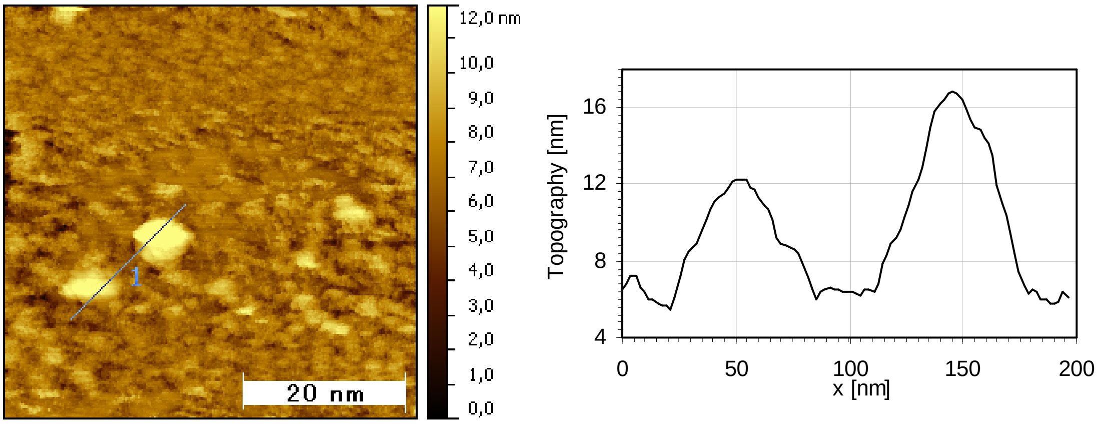

Figure 4.1 – Room-temperature STM topography scan of a Co/Al_2O_3/PEI surface with two (agglomerations of) nanoparticles visible (I = 50 pA, V = 3.0 V).

Figure 4.1 shows the result of a surface scan performed with very low current setpoint at high voltage, in order to obtain a large distance between sample and STM tip. Despite this large separation the image appears quite blurry, which is evidence of a considerably poor tip quality caused either by the tip crashing into the surface or particles or molecules being picked up by the tip. The large height of the two raised features shows that, if these details are FePt nanoparticles, they are probably agglomerated. The two details were only loosely adsorbed on the surface as they were no longer visible in a subsequent scan.

The difficulty of maintaining a good tip quality on these Co/Al_2O_3/PEI samples is caused by the thick tunneling barrier (Al_2O_3 and PEI) covering the cobalt electrode. To overcome this high tunneling resistance the STM tip needs to come closer to the surface, which increases the risk of the tip making physical contact with the surface when it encounters a high topographic feature during scanning. This problem was found to be strongly compounded when cooling the system to cryogenic temperature, to the point of tearing off several micrometers of material from the

PtIr needle during approach or while scanning. This temperature dependence indicates that conduction through the Al_2O_3/PEI barrier is dominated by thermally activated hopping. The lower thermal energy leads to an increase in the total resistance and forces the feedback loop to further decrease the tip-sample separation, causing the tip to make physical contact with the substrate. The intensity of tip breakdown also suggests that the PEI layer becomes stiffer at cryogenic temperatures, making the consequences of an STM tip crash much more severe.

Because of the above issues, the use of cobalt as a magnetic substrate layer was abandoned in favor of $La_{0.7}Sr_{0.3}MnO_3$ (LSMO). LSMO is an electrically conducting, perovskitic complex metal oxide that can be made to be ferromagnetic at room temperature [51]. The main advantage of using a conducting oxide is that the high surface stability obviates the need of a capping layer, eliminating about half of the barrier thickness that caused problems on the Co/Al2O3/PEI samples. LSMO specifically has the added advantage of being halfmetallic in bulk, meaning that the density of states at the Fermi level is (close to) 100% spin polarized. At the interface however, where the majority of electrons will tunnel, this polarization may be partially lost.

LSMO layers were epitaxially grown on two TiO_2-terminated $SrTiO_3$ (001) substrates (STO) using pulsed KrF laser ablation of a stoichiometric $La_{0.7}Sr_{0.3}MnO_3$ target, at a pulse rate of 5 Hz and a fluency of about 1.9 J/cm^2 across a spot of 2.42 mm^2. Deposition was performed in a $2.6 \cdot 10^{-1}$ mbar O_2 ambient at a temperature of 750° C, after which the samples were cooled down at about 10° C/min.

The material properties of LSMO grown in this fashion have been reported on in reference 51, which for a layer thickness above 15 unit cells (~6 nm) include low electrical resistivity ($<10^{-2}$ Ωcm, favorable for STM imaging), low magnetic coercivity (<25 Oe, allows easy magnetic switching of the layer) and high Curie temperature (>300 K, enables room temperature TMR experiments).

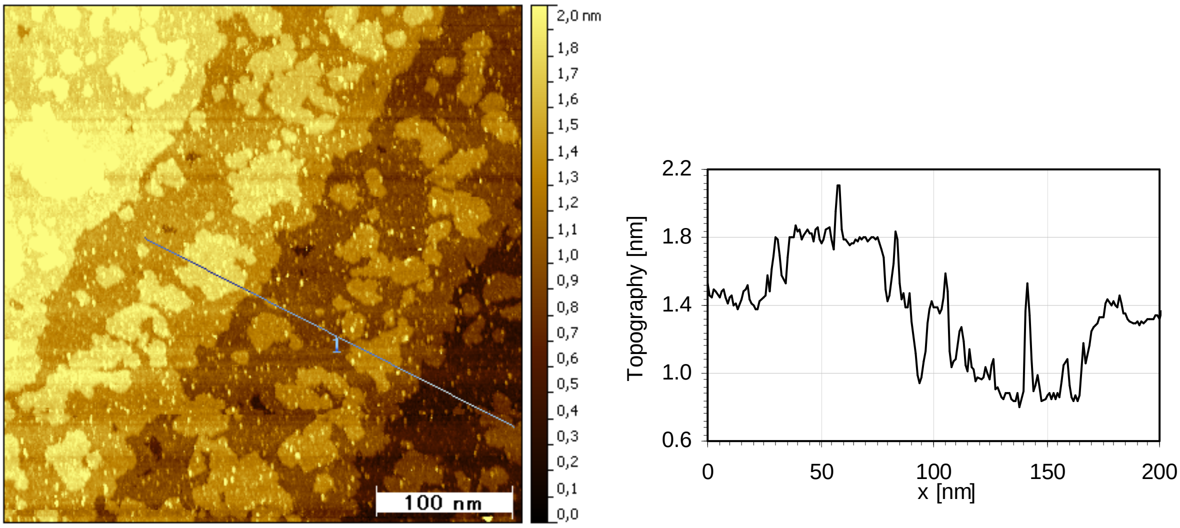

Figure 4.2 – Room-temperature STM scan of a 50 unit cell LSMO layer (I = 100 pA, V = 1.0 V) with height profile along the four 100-150 nm wide terraces, covered with large islands one unit cell in height (d ≈ 0.4 nm). A large number of nanometer-sized specks are also visible.

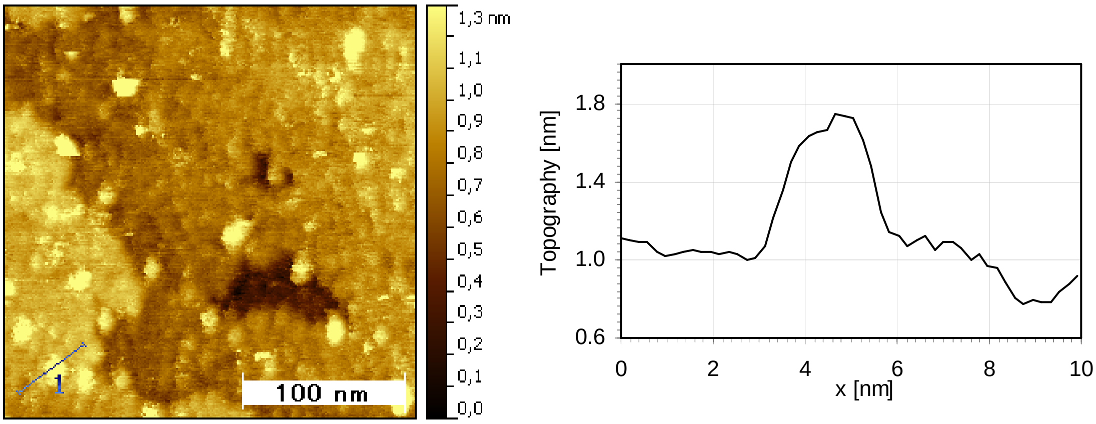

Figure 4.3 – Small-scale STM scan of a 50 unit cell LSMO layer (I = 100 pA, V = 1.0 V, room temperature) giving a more precise profile of the nanoislands covering the surface. The dimensions are of the same order of magnitude as those of the FePt nanoparticles.

The first LSMO sample was grown to a thickness of 50 unit cells (~20 nm), monitored by in-situ reflection high-energy electron diffraction (RHEED) measurements. The topography scan shown in Figure 4.2 reveals atomically flat terraces approximately 150 nm wide, covered by large island one unit cell in height ($d \approx 0.4$ nm). This shows that growth of the 51st layer had already commenced the moment deposition was halted. A large number of nanoislands are also visible, either one or two unit cells high, which are probably the first step in the formation process of mesoscale islands that, when joined together, form a new layer.

These nanoislands being only a little smaller than the FePt nanoparticles (Figure 4.3) gives rise to some concern for the usability of this substrate in SET experiments, as it may become difficult to distinguish the two in an STM topography scan. For this reason, the LSMO layer thickness on a second substrate was decreased to 20 unit cells (~8 nm), to obtain a smoother surface.

Due to an anomaly in the RHEED pattern it was decided during the growth process to halt deposition at the peak of the RHEED signal rather than the bottom. This led to the surface shown in Figure 4.4, a large number of interconnected islands forming a very open layer. Due to the non-continuous layer growth the number of nanoislands is difficult to compare to that of the earlier sample, but the difference does not appear to be very large.

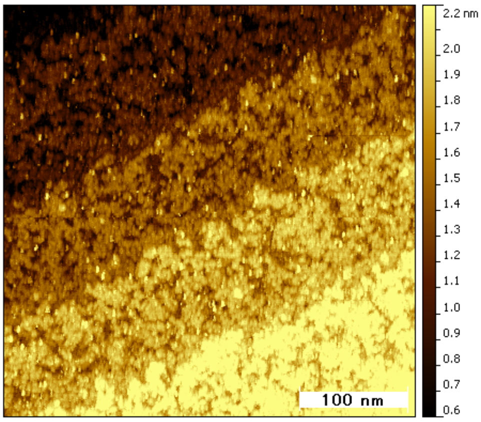

Figure 4.4 –STM topography scan of a 20 unit cell LSMO layer (I = 100 pA, V = 1.0 V, room temperature). Because deposition was stopped at a RHEED peak instead of at a bottom the top layer is grown only partially. The number of nanoislands does not appear to have been decreased with respect to the 50 unit cell layer.

The magnetic properties of the two LSMO layers as measured by VSM at room temperature are shown in Figure 4.5. It is visible that the total magnetization is independent of the angle of the (in-plane) applied field, which means that there is no in-plane easy axis in the material. The magnetic coercivity is very low, about equal to the resolution of the measurement (5 Oe), but the film does appear to be ferromagnetic at room temperature.

Comparing the results of the two samples reveals that the saturation magnetization of the thicker layer is 40% smaller than that of the thinner one (about 200 and 340 emu/cm^3, respectively). A similar saturation difference at room temperature was reported in reference [51] between 23 UC and 70 UC films (15% decrease). The Curie temperature of thin LSMO layers being relatively close to room temperature, this saturation anomaly may be related to the onset of superparamagnetic behavior.

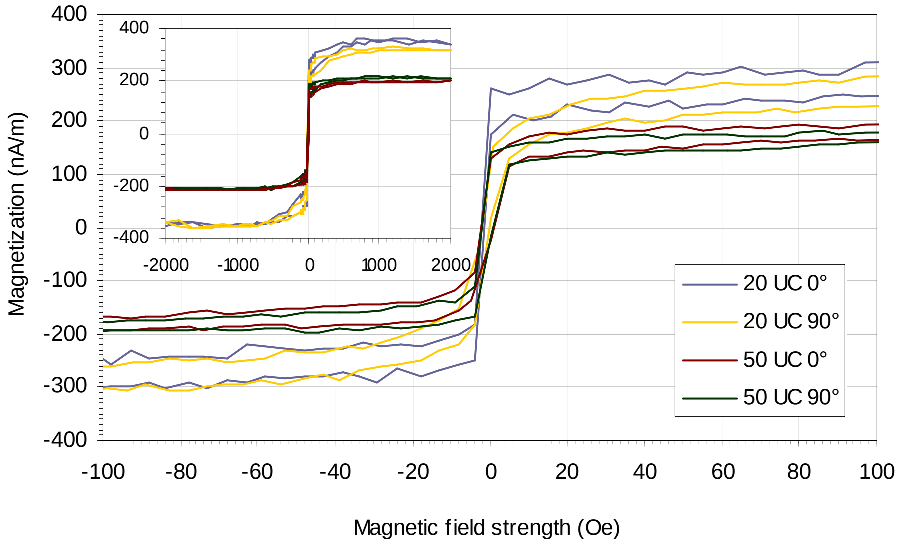

Figure 4.5 – Magnetic properties of two TiO_2/LSMO substrates measured using VSM at room temperature. There is very little angle dependence on the magnetization, and the coercivity is below the measurement resolution (5 Oe) in both cases. The inset shows the same graph at a larger field scale, showing that the thinner LSMO layer has a higher saturation magnetization.

Although the use of a magnetic substrate layer is an essential requirement for observing any spin valve-like behavior, this requirement does not apply to single-electron transport experiments. For this latter case it is therefore possible to use other substrates, specifically tailored to this application. A highly conductive substrate can be advantageous for investigation of conduction effects, as a higher density of states allows for a larger tip-sample separation at the same current setpoint. This can protect both the surface and the STM tip from damage.

In order to effectively distinguish isolated nanoparticles using STM, it is also preferable to have a substrate surface with very low roughness. For these reasons the SET experiments were performed on flame-annealed gold, which offers both very high conductivity and the property of forming large, atomically flat terraces on the order of several hundreds of nanometers wide. An added advantage of the flame-annealing process is that the high temperature flame helps remove contaminants from the gold surface [52,53].

The flame annealed gold samples used in this project’s experiments are prepared from prefabricated glass substrates with a >200 nm sputtered layer of gold (‘Gold arrandee’). These substrates are heated in a hydrogen flame for 5 minutes and then allowed to cool down to (close to) room temperature in air for 1 minute. Immediately after cooling the samples are submerged in a dithiol solution (see Section 3.2), in order to prevent surface contaminations from prolonged exposure in air. Figure 4.6 shows the typical structure of the flame annealed surface, consisting of flat terraces lying between slopes of many successive atomic steps ($d \approx 0.24$ nm). The observed terrace size lies between 40 and 200 nm.

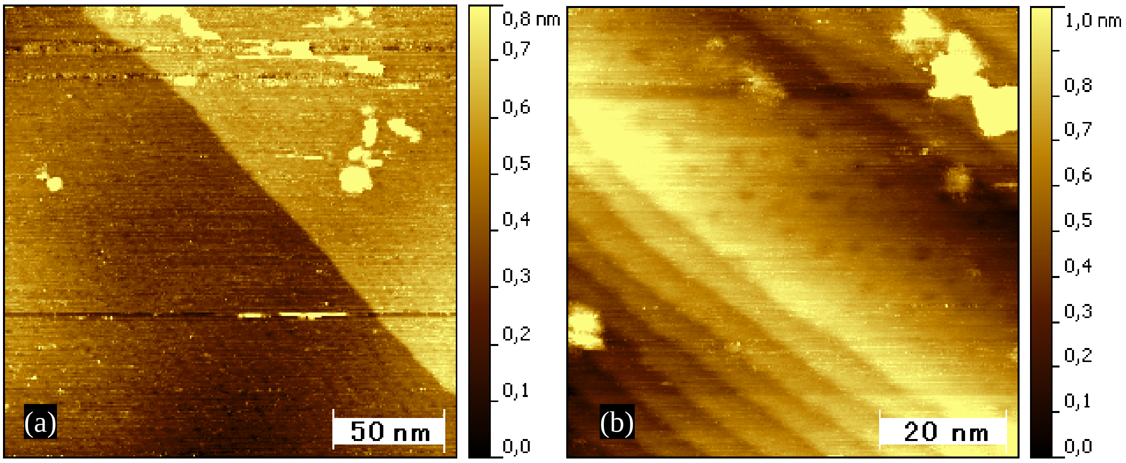

Figure 4.6 – Typical STM topography scans of a flame-annealed gold surface with C9 dithiol SAM (I = 100 pA, V = 0.1 V, room temperature). (a) Monatomic step separating two >200 nm terraces. (b) Many successive steps bordering an atomically flat terrace about 40 nm wide.

4.2 Experimental methods

In order to perform the single-electron tunneling experiments described in Chapter 2 a number of practical issues need to be considered. Since the working of a scanning tunneling microscope is based on a feedback loop keeping the tunneling current constant by adjusting the tip-sample separation, the first concern when measuring a current-voltage dependence is the need to prevent this feedback from reacting to the change in the tunneling current. For any *I*-*V* sweep the feedback must therefore be disengaged until the voltage sweep is completed, in order to keep the tip at a constant height from the sample.

In theory, the tunneling current should exactly return to the current setpoint once the voltage sweep is completed and the bias is returned to its operational value. In practice this is however never the case, as thermal, mechanical and electrical fluctuations in the STM will always lead to a changing tip-sample separation during the measurement. In particular any fluctuation in the Z-piezo will directly lead to a change in tip-sample separation, greatly affecting the tunneling current. Only when the feedback loop is reengaged can the STM compensate for these drifts and will the tip height return to its previous value.

Figure 4.7 shows the flow and timing diagram of a typical *I*-*V* measurement. The moment the feedback is disengaged the software begins ramping the bias voltage to the selected starting value. After a short stabilization time the bias is swept through the measurement range at a set ramp rate, pausing at set intervals where the current signal is to be sampled. At each measurement point the system can be set to wait for a pre-sample delay before the current is measured. A measurement point can also be averaged over a number of samplings to increase the signal to noise ratio.

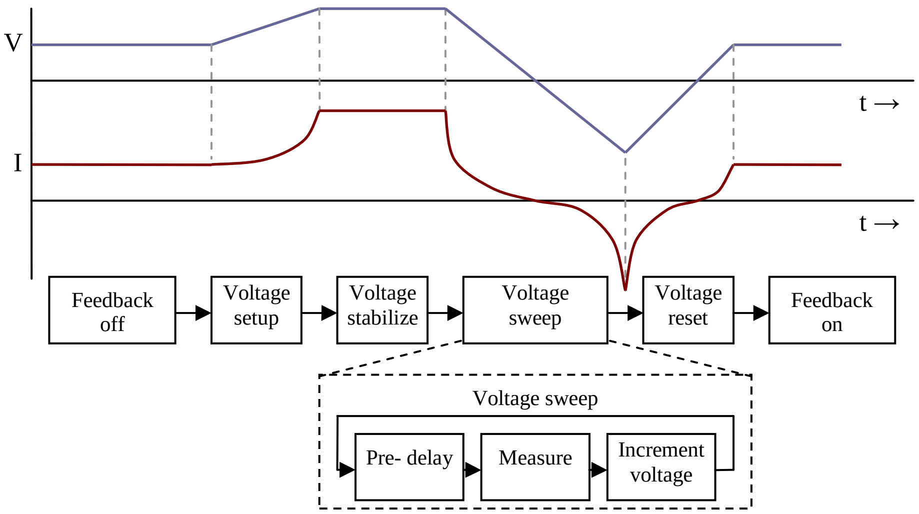

Figure 4.7 – Flow diagram of a current-voltage spectroscopic measurement.

Once the measurement sweep is finished, the voltage is returned to the bias setpoint and the feedback loop is reengaged. When acquiring multiple sweeps in sequence, a waiting period can be set to allow the feedback loop to stabilize the tunneling current in between measurements.

As mentioned previously it is essential to note that the stability of the tunneling current can be greatly impaired by drifting effects once the feedback loop is disabled. This means that for a reliable *I-V* measurement the total measurement time should be kept as short as possible. The settings used in this project are listed in Table 4.1. By using a large setup and sweep rate a larger fraction of the measurement time can be spent on actual sampling. Using the printed settings a measurement containing 81 data points can be executed in about 100 ms, which is in most cases sufficient to prevent destabilization of the tip.

Table 4.1 – Timing parameters for I-V spectroscopic measurements.

Samples per point	50
Pre-sample delay	400 µs
Sampling time	5 µs
Voltage stabilization	10 ms
Voltage setup rate	100 V/s
Voltage sweep rate	50 V/s

A second consideration for practical SET experiments is the bias and current setpoint settings used during measurements. Because the Coulomb blockade effect is visible symmetrically around zero bias, the settings must be such that even at low bias the tunneling current remains measurable. For a large bias setpoint in combination with a small current setpoint the tip-sample separation can be so great that, as the voltage is sweeped down, the current signal will drop to zero regardless of whether or not an actual blockade is reached.

Figure 4.8 illustrates this problem, showing two *I-V* measurements on a Co/Al_2O_3/PEI surface which, due to the thick barrier layer, were measured at a high bias setpoint and very low current setpoint. In both cases the measured current goes to zero when the voltage drops to about one third of the setpoint. This shows that this is not the Coulomb blockade effect, as the threshold voltage should be independent of the bias setpoint (Equation (2.3)).

In order to prevent this problem, the bias setpoint should be kept on the order of the expected blockade voltage. To sweep a larger range it is possible to start measuring at a voltage higher than the bias setpoint, using the voltage setup step in Figure 4.7.

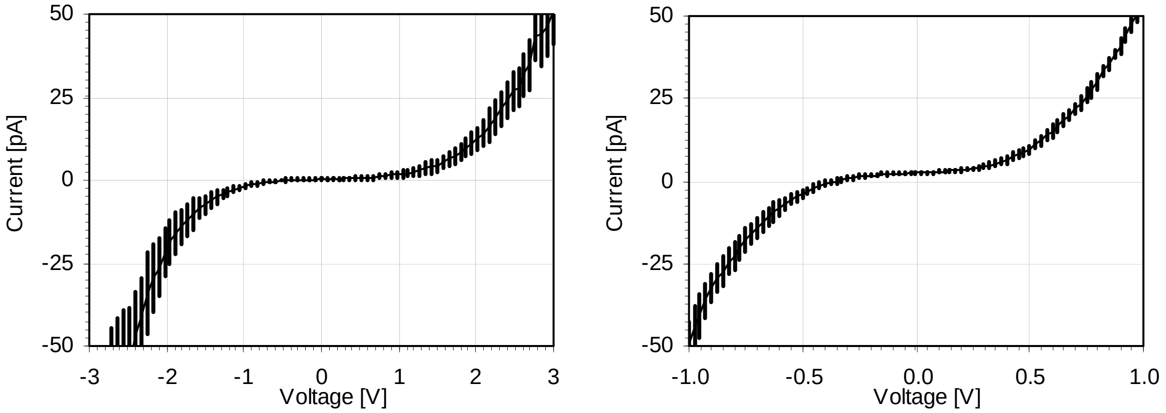

Figure 4.8 – Room-temperature current-voltage spectroscopy measurements at a current setpoint of 50 pA and a bias setpoint of 3 V (left) and 1 V (right). Both curves are averaged over 10 measurements, with the standard deviation shown as vertical bars. In both cases the current approaches zero when the voltage drops below one third of the bias setpoint, showing that this is not the Coulomb blockade effect but rather a loss of tunneling current due to too large tip-sample separation.

Similar to sweeping the voltage in SET measurements, spin-dependent transport experiments in an STM consist of sweeping the magnetic field while measuring the tunneling current. In the equipment used in this project the magnetic field is applied by running DC current through a Helmholtz coil pair, controlled by two 400W power supplies. Because these power supplies experience a very heavy inductive load the switching speed of the magnetic field is limited by the maximum voltage output (±50 V).

For the coils in use it was found that using the parameters listed in Table 4.2 a field sweep can be executed that takes about half a second and reaches a peak coil current of about 1.2 A. The magnetic field strength at this current was measured to be 13.6 Oe outside of the vacuum chamber. Because Helmholtz coils are designed to minimize the non-uniformity of the magnetic field between the coil planes, the field at the sample holder (inside the vacuum chamber) can be expected to be similar to the measured value.

As was shown in Figure 4.5 the room temperature coercivity of the LSMO layers is well beneath 10 Oe, meaning that reversing the substrate layer magnetization for TMR measurements at that temperature is possible with the settings shown. For experiments at $T \approx 40$ K a slightly stronger field may be required, as the coercivity of LSMO layers of at least 20 UC at $T = 10$ K was reported to be about 20 Oe [51].

Table 4.2 – Timing parameters for I-V spectroscopic measurements.

Samples per point	25
Pre-sample delay	200 µs
Sampling time	5 µs
Voltage stabilization	0 ms
Control signal to BOP 50-8M power supply	1.85 V to -1.85 V, 47mV step, bidirectional sweep
Control signal setup rate	50 V/s
Control signal sweep rate	50 V/s

In order to facilitate spin transfer torque experiments a spin-polarized tunneling current can be injected into the nanoparticle by reversing the STM bias voltage, so that electrons no longer tunnel from the STM tip but from the magnetic substrate. As was mentioned in Section 2.6, a typical current density required for spin transfer torque switching is on the order of 10^7 A/cm^2. If we assume that the tunneling current flows across the entire cross-sectional surface area of a 3 nm nanoparticle, an estimate for the required switching current can be calculated to be $I_S = J_S \cdot \pi \cdot r^2 \approx 10^{-6}$ A.

The STM equipment used in this project is designed to operate at setpoint currents up to 10 nA, meaning that with standard equipment the switching current density probably cannot be reached. This problem may be alleviated by applying a magnetic field to partially reorient the nanoparticle magnetization, lowering the energy barrier required for spin torque switching. The maximum field strength available in the used setup is however on the order of 100 Oe, which is much lower than the saturation field strength of the nanoparticles (see Figure 3.2), so a large current may still be required in this case.

Lowering the energy barrier for magnetization switching is also possible by increasing the thermal energy through local heating of the nanoparticle. Joule heating caused by large local current densities has been reported to aid STM-based spin torque switching of Fe nanoislands grown on a W surface, which however still required a spin-polarized current pulse on the order of 10^{-6} A for ~100 ms to switch magnetization [54]. An unpolarized current pulse of the same magnitude was also reported to be able to revert the magnetization in most cases, which means that reverting the nanoparticle magnetization can be done either by switching the magnetization of the substrate or by reversing the direction of current flow (from the STM tip).

It should however be noted that, since all conduction to and from an isolated nanoparticle occurs through tunneling, there may not be enough local, classical flow of electrons in the nanoparticle to cause significant Joule heating. If electron-phonon interactions are not likely to occur in the island, the electrons will not be able to transfer any energy before they tunnel out. In this case all Joule heating will take place in the substrate and STM tip, where the energy can easily flow away into the bulk.

4.3 Single electron tunneling experiments

The first evidence of single-electron tunneling was obtained on a flame-annealed gold sample with C9 dithiol SAM. The *I-V* curves shown in Figure 4.9 are each averaged over 5 measurements at the same location, performed at room temperature. All spectra are measured during topographic imaging, meaning that the STM tip scanning the surface is paused for a short time while the spectrum is measured, after which the topographic scan continues from the same location. This enables very accurate control of the location where each spectrum is measured, as there is no time for drifting processes to influence the tip position.

The on-particle and off-particle curves reveal a significant shape difference, with the on-particle spectrum showing lower current at low voltages ($V < 0.1$ V). At higher voltages the two curves cross and the on-particle current becomes higher than the off-particle current. The two curves remain separated even after considering the standard deviation of the measurement averaging, particularly at low voltages.

These results are verified in repeat measurements, both at the same and at different locations. This suggests that at room temperature the nanoparticle are at the onset of Coulomb blockade, in this case with a threshold voltage of approximately 0.1 V. The Coulomb charging energy would then be 0.2 eV, which is within reasonable range of the estimated 90 meV for a 4 nm nanoparticle in Section 2.4.

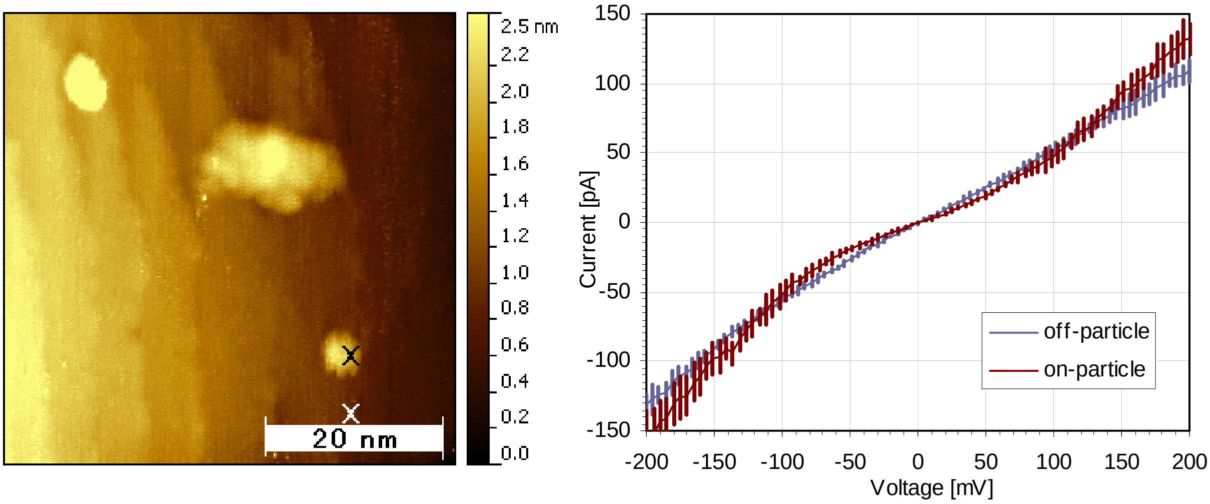

Figure 4.9 – Room-temperature STM topography scan of FePt nanoparticles on flame-annealed gold with C9 dithiol SAM (I = 50 pA, V = 0.1 V), with I-V spectroscopy measurements performed at the marked locations. Both I-V curves are averaged over 5 measurements, with the standard deviation shown as vertical bars. The on-particle spectra show a lower current at low voltage, suggesting partial Coulomb blockade.

Similar spectroscopic measurements were performed, on the same sample, after cooling down the system to $T \approx 40$ K. The spectroscopic curves in Figure 4.10 show clear Coulomb blockade behavior of the nanoparticle, with the slope at zero voltage virtually flat (zero conduction). The topography profile of the nanoparticle has been presented before in Figure 3.13a, showing a height of 0.8 nm.

Apart from the Coulomb blockade, also the Coulomb staircase is observed in this measurement. The on-particle *I-V* curve is repeated in Figure 4.11 together with a plot of the derivative of the tunneling current, *dI/dV*. At each point where the derivative approaches zero the electrons are blocked from tunneling by the electrons occupying the nanoparticle at that energy level (voltage).

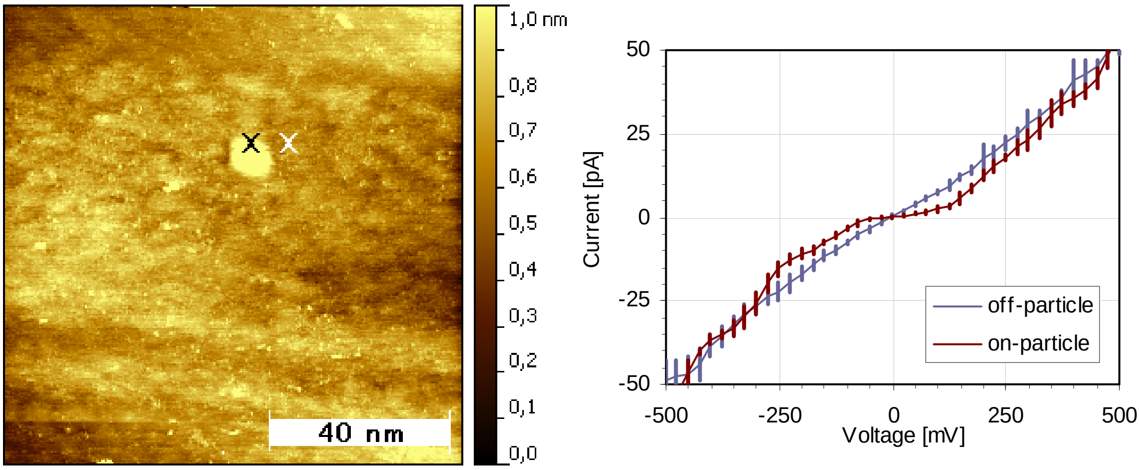

Figure 4.10 – Low-temperature STM topography scan of FePt nanoparticles on flame-annealed gold with C9 dithiol SAM (I = 50 pA, V = 0.5 V, T ≈ 40 K), with I-V spectroscopy measurements performed at the marked locations (5 averages, standard deviation shown as vertical bars).

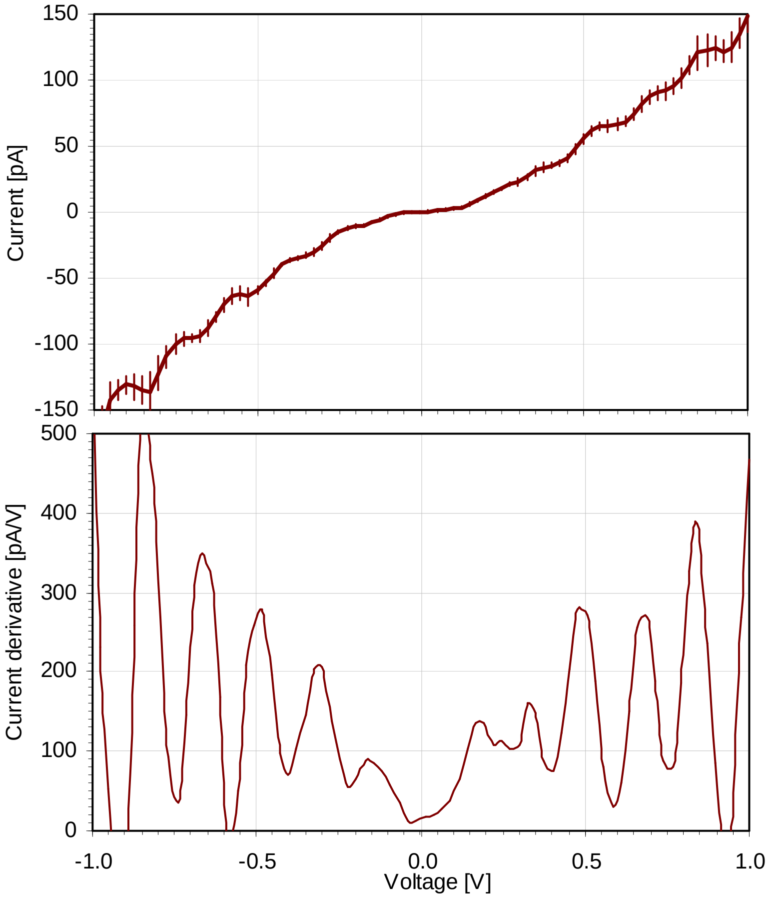

Figure 4.11 – On-particle I-V spectrum of an FePt nanoparticle at $T \approx 40$ K , repeated from Figure 4.10, plotted with its 3-points numerical derivative. The conductivity peaks are spaced approximately 0.15 V apart.

The Coulomb staircase allows us to easily extrapolate the Coulomb charging energy and from that calculate the capacitance of the nanoparticle. The peaks in the current derivative plot of Figure 4.11 are spaced approximately 0.15 V apart. At these peaks the conductivity is high, meaning that the tunneling electrons have enough energy to overcome an extra unit of charging energy e^2/C. This allows conduction to go from single electron tunneling to double electron tunneling, then to triple electron tunneling, and so on.

This means the Coulomb charging energy of the nanoparticle is 0.15 eV, which is close to the results obtained at room temperature and very reasonable when compared to the 90 meV estimated for a 4 nm nanoparticle. Using Equation (2.4) the total capacitance of the double tunnel junction can be calculated to be $C \approx 1.1$ aF.

An immediate repeat measurement at the same nanoparticle gives the *I-V* spectra shown in Figure 4.12. The separation between the on-particle and off-particle curves is particularly clear in this measurement and the previously obtained blockade voltage is verified ($V_{CB} = 2 \cdot V_{th} \approx 0.15$ V). The fact that the Coulomb staircase is no longer visible means that the inbound tunneling resistance has become high compared to the outbound resistance (see Section 2.2). It may be that the nanoparticle was moved by the STM tip, decreasing the outbound resistance. In order to maintain a constant tunneling current the STM feedback loop would then have to increase the tip-sample separation, increasing the inbound tunnel resistance and thus amplifying the initial change.

During the course of the STM experiments, the Coulomb blockade was observed at $T \approx 40$ K on more than ten different nanoparticles. In all cases the result was reproducible by immediately repeating the measurement, and identical results were obtained for over 10 repeat measurements on some nanoparticles. The Coulomb blockade could be readily achieved at cryogenic temperatures for almost all nanoparticles found by STM imaging. This is probably because the particle size distribution quickly drops to zero for diameters greater than 4 nm (see Figure 3.1), meaning that the Coulomb charging energy is greater than the thermal energy in almost all cases. It also illustrates the importance of strong nanoparticle anchoring, as finding immobile particles seems to be the limiting factor in this experiment.

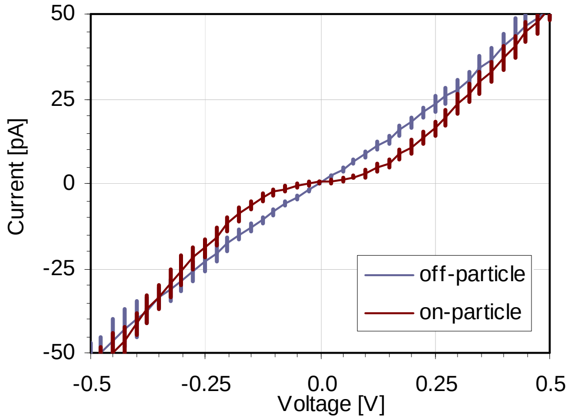

Figure 4.12 – On and off-particle I-V spectra, measured at the locations marked in Figure 4.10 (I = 50 pA, V = 0.5 V, T ≈ 40 K). Each curve is averaged across 20 measurements, with the standard deviation shown as vertical bars. The threshold voltage is approximately 75 mV.

4.4 Magnetic substrates

As has been explained in Section 4.1, the samples used for magnetic experiments are based on STO/LSMO substrates in order to decrease the barrier thickness and thus the tunneling resistance. The effectiveness of LSMO can be determined by comparing the topography scan results to those of the Co/Al_2O_3 samples. Figure 4.13 shows a room-temperature and low-temperature STM topography image of the 20 UC LSMO sample covered with PEI, using a newly cut STM tip for both scans. Comparing these images to the scans of the empty samples (Figure 4.4, without PEI) the results are decidedly less clear, but the large-scale surface structure is still resolved in both cases.

In the room-temperature scan (Figure 4.13a) the open structure of the half-grown top layer is partially visible, as are a large number of nanoscale details that appear to be the nanoislands seen before on the clean surface. At low temperature however most of these details appear to be washed out by tip bluntness, which can be recognized by the almost closed appearance of the LSMO layer. This indicates that tip degradation is still a severe problem when using PEI as an anchoring layer, even on LSMO substrates. The increased noise visible in Figure 4.13b shows that, similar to the results on cobalt, more tip damage is incurred during low-temperature scanning.

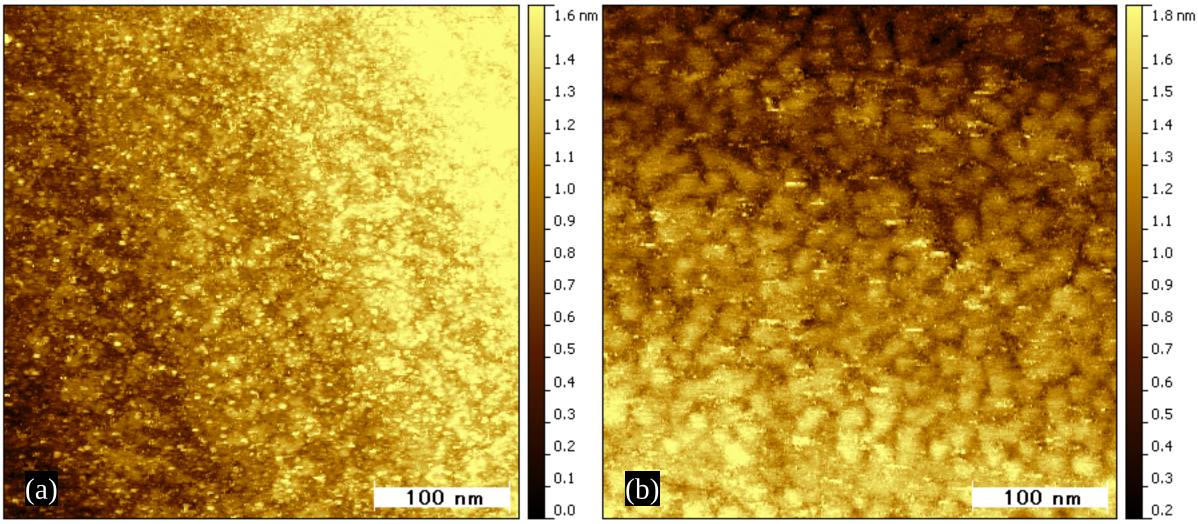

Figure 4.13 – STM topography scans of a 20 UC LSMO layer covered with a PEI layer and isolated FePt nanoparticles (I = 100 pA, V = 1.0 V). (a) Room-temperature scan showing the open structure of the half-grown top layer, as well as sparse nanoisland growth. (b) Low-temperature scan showing evidence of a blunted tip (T ≈ 40 K).

On the 50 UC sample a similar problem occurs, as is shown by the scan result in Figure 4.14. In this scan the tip can actually be seen to degrade as the scan progresses, with the noise level strongly increased further down in the image. From this it can be concluded that the tunnel barrier is still too thick to allow good quality scan images to be made. Nevertheless the results are much better than what has been obtained on the Co/Al_2O_3 samples, which could not be imaged at all. This shows that decreasing barrier thickness is the main concern for these experiments.

Because of the very short STM tip lifetime on these samples it was not possible to find isolated, immobilized nanoparticles on the substrate surface for spin-dependent transport experiments. Mobile nanoparticles were however observed, which verifies the conclusion made in Section 3.4 that the anchoring of FePt nanoparticles on PEI is not very strong.

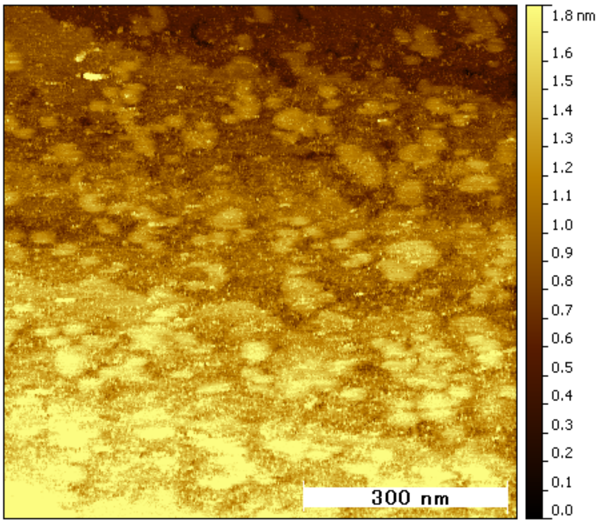

Figure 4.14 – STM topography scan of a 50 UC LSMO layer covered with a PEI layer and isolated FePt nanoparticles (I = 100 pA, V = 1.0 V, T ≈ 40 K). The tip quality can be seen to degrade as the scan progresses (from the top downwards).

5 Conclusions and recommendations

The goal of this project was to investigate the electron transport properties of FePt nanoparticles using STM spectroscopy, focusing on single-electron tunneling (Coulomb blockade) behavior and spin-dependent transport (TMR measurements). For this the isolation of nanoparticles on various surfaces was investigated and achieved through control of the nanoparticle dispersion concentration and the submergence time of adhesive substrates in this dispersion. The results were verified by STM topographic and spectroscopic measurements. For single-electron experiments highly conductive gold surfaces were fabricated, while for TMR experiments cobalt and LSMO surfaces were fabricated as ferromagnetic substrates.

To obtain particle immobilization on gold substrates a C9 dithiol SAM was applied as adhesion layer. Nanoparticle anchoring was found to be strong enough to allow spectroscopic measurements, although the immobile particles appeared to be partially embedded in the SAM. This is an unwanted effect, as a decreased particle-substrate separation leads to a higher outbound tunneling rate Γ_{out}, which is at odds with the requirement for observing the Coulomb staircase ($\Gamma_{in} >> \Gamma_{out}$, see Section 2.2).

It is possible that a better particle immobilization can be obtained using molecules with a longer alkyl chain. The C9 dithiol molecule is significantly smaller than the oleic acid and oleyl amine surfactants on the nanoparticle, which may make the ligand exchange process more difficult. On the other hand longer dithiol molecules may give rise to a stronger prevalence of the looping phase during SAM adsorption, so care should be taken to maintain the desired (standing-up) growth mode. A longer alkyl chain will also lead to a thicker adhesion layer with a higher tunnel resistance, so the chain length should be optimized such that the tunnel resistance is low enough to allow STM imaging.

On metal oxide substrates a thin PEI layer was used to immobilize nanoparticles. Using STM topographic imaging it was observed that anchoring of individual particles on PEI was very poor, whereas the self-assembly of a particle monolayer on PEI was quite effective. This suggests that interaction between the particles helps the physical stabilization.

Low-temperature STM topography imaging of substrates with PEI was found to be very difficult due to severe tip degradation. This is most probably caused by the feedback loop approaching the tip too closely to the surface, trying to overcome the high tunneling resistance of the ~3 nm PEI barrier.

In view of the success of the C9 dithiol system, a better performance should be obtainable by using a self-assembled monolayer of molecules with for example phosphate groups to bond to an oxide substrate, as described in reference [32], and thiol termination to bond to an FePt particle. The thiol groups should allow for better particle immobilization than observed on PEI, while the reduced thickness of a molecular monolayer will allow the STM tip to approach to tunneling range without making contact with the surface.

Using STM spectroscopy the Coulomb blockade of more than ten different FePt nanoparticles on flame-annealed gold / C9 dithiol SAM surfaces was observed reproducibly at low temperatures ($T \approx 40$ K), and a clear Coulomb staircase was measured. Using the latter result the Coulomb charging energy of that nanoparticle was found to be approximately 0.15 eV, corresponding to a total junction capacitance of ~1.1 aF. At room temperature a significant and reproducible difference between on-particle and off-particle *I-V* spectra suggests the onset of Coulomb blockade, with a charging energy estimated at ~0.2 eV. Both results are in good agreement with the estimated charging energy of a 4 nm nanoparticle, $E_C > 90$ meV.

On the magnetic Co/Al_2O_3/PEI and LSMO/PEI substrates no isolated nanoparticles were found with strong enough anchoring to allow *I-V* spectroscopy measurements. This means that improving the adhesion layer is the most important requirement for future magnetic experiments. The properties of LSMO (chemical stability, low coercivity, strong spin polarization) make it a more interesting choice than cobalt, especially because cobalt requires a protective oxide layer which increases the tunnel resistance.

It was found that the measurement setup used in this project can supply a magnetic field strength of >13 Oe if sweeping the field for about 0.5 s. The room temperature coercivity of the LSMO layer was measured to be below 5 Oe, but a slightly stronger field may be required for switching the layer at low temperature. The maximum time the feedback loop can be disengaged before tip-sample separation drift effects become disruptive was found to be ~100 ms, so the sweep rate will probably have to be increased as well. This means that stronger Helmholtz coil power supplies will probably be required to support the TMR measurements described in this report.

The monodomain structure and favorable magnetic and chemical properties make FePt nanoparticles interesting candidates for future magnetic data storage systems such as highly integrated MRAM. To further assess their applicability in this context it is very interesting to investigate spin transfer torque switching of the nanoparticles using a spin-polarized current tunneling from the substrate. The required current densities for full current-driven switching are not trivial to obtain in the STM equipment used in this project, so the use of field assisted or thermally assisted switching may be more viable solutions.

6 Literature

1. G. Binasch, P. Grünberg, F. Saurenbach, and W. Zinn, "*Enhanced magnetoresistance in layered magnetic structures with antiferromagnetic interlayer exchange*," Physical Review B, Vol. 39, pp. 4828-4830 (1989)
2. M.N. Baibich, J.M. Broto, A. Fert, F. Nguyen Van Dau, F. Petroff, P. Etienne, G. Creuzet, A. Friederich and J. Chazelas, "*Giant Magnetoresistance of (001)Fe/(001)Cr Magnetic Superlattices*," Physical Review Letters, Vol. 61, pp. 2472-2475 (1988)
3. S.A. Wolf, D.D. Awschalom, R.A. Buhrman, J.M. Daughton, S. von Molnar, M.L. Roukes, A.Y. Chtchelkanova and D.M. Treger, "*Spintronics: A Spin-Based Electronics Vision for the Future*," Science, Vol. 294, pp. 1488-1495 (2001)
4. J.F. Gregg, I. Petej, E. Jouguelet and C. Dennis, "*Spin electronics - a review*," Journal of Physics D: Applied Physics, Vol. 35, pp. R121-R155 (2002)
5. J.M. Daughton, "*Magnetoresistive memory technology*," Thin Solid Films, Vol. 216, pp. 162-168 (1992)
6. S. Tehrani, J.M. Slaughter, E. Chen, M. Durlam, J. Shi and M. Deherrera, "*Progress and Outlook for MRAM Technology*," IEEE Transactions on Magnetics, Vol. 35, pp. 2814-2819 (1999)
7. "*Everspin Technologies takes MRAM to higher densities with 16 megabit product introduction*," press release, http://www.everspin.com (2010)
8. "*Freescale Leads Industry in Commercializing MRAM Technology*," press release, http://www.freescale.com (2006)
9. D. Weller and A. Moser, "*Thermal effect limits in ultrahigh-density magnetic recording*," IEEE Transactions on Magnetics, Vol. 35, pp. 4423-4439 (1999)
10. R.L. White, R.M.H. Newt and R.F.W. Pease, "*Patterned media: a viable route to 50 Gbit/in2 and up for magnetic recording?*" IEEE Transactions on Magnetics, Vol. 33, pp. 990-995 (1997)
11. S. Sun, S. Anders, T. Thomson, J.E.E. Baglin, M.F. Toney, H.F. Hamann, C.B. Murray and B.D. Terris, "*Controlled Synthesis and Assembly of FePt Nanoparticles*," Journal of Physical Chemistry B, Vol. 107, pp. 5419-5425 (2003)
12. J. Barnas and A. Fert, "*Magnetoresistance Oscillations due to Charging Effects in Double Ferromagnetic Tunnel Junctions*," Physical Review Letters, Vol. 80pp. 1058-1061 (1998)
13. H. Brückl, G. Reiss, H. Vinzelberg, M. Bertram, I. Mönch and J. Schumann, "*Enhanced magnetoresistance of permalloy/Al-oxide/cobalt tunnel junctions in the Coulomb blockade regime*," Physical Review B, Vol. 58, pp. R8893-R8896 (1998)
14. S. Takahashi and S. Maekawa, "*Effect of Coulomb Blockade on Magnetoresistance in Ferromagnetic Tunnel Junctions*," Physical Review Letters, Vol. 80pp. 1758-1761 (1998)
15. M. Hosomi, H. Yamagishi, T. Yamamoto, K. Bessho, Y. Higo, K. Yamane, H. Yamada, M. Shoji, H. Hachino, C. Fukumoto, H. Nagao and H. Kano, "*A novel nonvolatile memory with spin torque transfer magnetization switching: Spin-RAM*," International Electron Devices Meeting 2005 Technical Digest, pp. 459-462 (2005)
16. T. Kishi, H. Yoda, T. Kai, T. Nagase, E. Kitagawa, M. Yoshikawa, K. Nishiyama, T. Daibou, M. Nagamine, M. Amano, S. Takahashi, M. Nakayama, N. Shimomura, H. Aikawa, S. Ikegawa, S. Yuasa, K. Yakushiji, H. Kubota, A. Fukushima, M. Oogane, T. Miyazaki and K. Ando, "*Lower-current and fast switching of a perpendicular TMR for high speed and high density spin-transfer-torque MRAM*," International Electron Devices Meeting 2008 Technical Digest, pp. 1-4 (2008)
17. U. Meirav and E.B. Foxman, "*Single-electron phenomena in semiconductors*," Semiconductor Science and Technology, Vol. 11, pp. 255-284 (1996)
18. H. Tsuji, N. Arai, T. Matsumoto, K. Ueno, Y. Gotoh, K. Adachi, H. Kotaki and J. Ishikawa, "*Silver nanoparticle formation in thin oxide layer on silicon by silver-negative-ion implantation for Coulomb blockade at room temperature*," Applied Surface Science, Vol. 238, pp. 132-137 (2004)
19. C. Gao, F. Duewer and X.-D. Xiang, "*Quantitative microwave evanescent microscopy*," Applied Physics Letters, Vol. 75, pp. 3005-3007 (1999)
20. K. Yoon, K. Kim, J. Koo, J. Yang, Y.H. Do, J. Kwak and J. Hong, "*Spin-Polarized Transport Phenomena in Double Magnetic Tunnel Junctions Caused by Ferromagnetic CoFe Nanoparticles*," IEEE Transactions on Magnetics, Vol. 46, pp. 7-9 (2010)

21. H. Sukegawa, S. Nakamura, A. Hirohata, N. Tezuka and K. Inomata, "*Significant Magnetoresistance Enhancement due to a Cotunneling Process in a Double Tunnel Junction with Single Discontinuous Ferromagnetic Layer Insertion*," Physical Review Letters, Vol. 94, 068304-1-068304-4 (2005)
22. S. Woedtke, Ph.D. thesis, Institut für Experimentelle und Angewandte Physik der Universität Kiel (2002)
23. A. Russell, "*The Capacity Coefficients of Spherical Electrodes*," Proceedings of the Physical Society of London, Vol. 23, pp. 352-360 (1911)
24. I. Zutic, J. Fabian and S. Das Sarma, "*Spintronics: Fundamentals and applications*," Reviews of Modern Physics, Vol. 76, pp. 323-410 (2004)
25. J.C. Slonczewski, "*Conductance and exchange coupling of two ferromagnets separated by a tunneling barrier*," Physical Review B, Vol. 39, pp. 6995-7002 (1989)
26. C. Wasshuber, "*About Single-Electron Devices and Circuits*," Dissertation, Technischen Universitat Wien (1997)
27. L. Berger, "*Emission of spin waves by a magnetic multilayer traversed by a current*," Physical Review B, Vol. 54, pp. 9353-9358 (1996)
28. J.C. Slonczewski, "*Current-driven excitation of magnetic multilayers*," Journal of Magnetism and Magnetic Materials, Vol. 159, pp. L1-L7 (1996)
29. G.D. Fuchs, N.C. Emley, I.N. Krivorotov, P.M. Braganca, E.M. Ryan, S.I. Kiselev, J.C. Sankey, D.C. Ralph, R.A. Buhrman and J.A. Katine, "*Spin-transfer effects in nanoscale magnetic tunnel junctions*," Applied Physics Letters, Vol. 85, pp. 1205-1207 (2004)
30. K. Yakushiji, S. Yuasa, T. Nagahama, A. Fukushima, H. Kubota, T. Katayama and K. Ando, "*Spin-Transfer Switching and Thermal Stability in an FePt/Au/FePt Nanopillar Prepared by Alternate Monatomic Layer Deposition*," Applied Physics Express, Vol. 1, pp. 041302-1-041302-3 (2008)
31. D.C. Ralph and M.D. Stiles, "Spin transfer torques," Journal of Magnetism and Magnetic Materials, Vol. 320, pp. 1190-1216 (2008)
32. O. Yildirim, T. Gang, S. Kinge, D.N. Reinhoudt, D.H.A. Blank, W.G. van der Wiel, G. Rijnders and J. Huskens, "*Monolayer-directed Assembly and Magnetic Properties of FePt Nanoparticles on Patterned Aluminum Oxide*," International Journal of Molecular Sciences, Vol. 11, pp. 1162-1179 (2010)
33. S. Sun, "*Recent Advances in Chemical Synthesis, Self-Assembly, and Applications of FePt Nanoparticles*," Advanced Materials, Vol. 18, pp. 393-403 (2006)
34. R.P. Andres, T. Bein, M. Dorogi, S. Feng, J.I. Henderson, C.P. Kubiak, W. Mahoney, R.G. Osifchin and R. Reifenberger, "*Coulomb Staircase at Room Temperature in a Self-Assembled Molecular Nanostructure*," Science, Vol. 272, pp. 1323-1325 (1996)
35. T. Ohgi, H.-Y. Sheng, Z.-C. Dong, H. Nejoh and D. Fujita, "*Charging effects in gold nanoclusters grown on octanedithiol layers*," Applied Physics Letters, Vol. 79, pp. 2453-2455 (2001)
36. S. Kohale, S.M. Molina, B.L. Weeks, R. Khare and L.J. Hope-Weeks, "*Monitoring the Formation of Self-Assembled Monolayers of Alkanedithiols Using a Micromechanical Cantilever Sensor*," Langmuir, Vol. 23, pp. 1258-1263 (2007)
37. H.B. Akkerman, A.J. Kronemeijer, P.A. van Hal, D.M. de Leeuw, P.W.M. Blom and B. de Boer, "*Self-Assembled-Monolayer Formation of Long Alkanedithiols in Molecular Junction*," Small, Vol. 4, pp. 100-104 (2008)
38. C.D. Bain, E.B. Troughton, Y.-T. Tao, J. Evall, G.M. Whitesides and R.G. Nuzzo, "*Formation of monolayer films by the spontaneous assembly of organic thiols from solution onto gold*," Journal of the American Chemical Society, Vol. 111, pp. 321-335 (1989)
39. A. Ulman, "*Formation and Structure of Self-Assembled Monolayers*," Chemical Review, Vol. 96, pp. 1533-1554 (1996)
40. D. Qu, B.-C. Kim, C.-W.J. Lee and K. Uosaki, "*1,n-Alkanedithiol (n = 2, 4, 6, 8, 10) Self-Assembled Monolayers on Au(111): Electrochemical and Theoretical Approach*," Bulletin of the Korean Chemical Society, Vol. 30, pp. 2549-2554 (2009)
41. M. Brückner, B. Heinz and H. Morgner, "*Molecular orientation in organic monolayers probed by UPS and MIES (metastable induced electron spectroscopy)*," Surface Science, Vol. 319, pp. 370-380 (1994)
42. P. Kohli, K.K. Taylor, J.J. Harris and G.J. Blanchard, "*Assembly of Covalently-Coupled Disulfide Multilayers on Gold*," Journal of the American Chemical Society, Vol. 120, pp. 11962-11968 (1998)

43. Y.-L. Loo, J.W.P. Hsu, R.L. Willett, K.W. Baldwin, K.W. West and J.A. Rogers, "*High-resolution transfer printing on GaAs surfaces using alkane dithiol monolayers*," Journal of Vacuum Science and Technology B, Vol. 20, pp. 2853-2856 (2002)
44. M. Yanga and Z. Zhang, "*Impediment to heterogeneous electron transfer reactions of redox-active species by alkanedithiol self-assembled monolayers with and without an adlayer of Au nanoparticles*," Electrochimica Acta, Vol. 49, pp. 5089-5095 (2004)
45. S. Maenosono and S. Saita, "*Theoretical assessment of FePt nanoparticles as heating elements for magnetic hyperthermia*," IEEE Transactions on Magnetics, Vol. 42, pp. 1638-1642 (2006)
46. M.S. Seehra, V. Singh, P. Dutta, S. Neeleshwar, Y.Y. Chen, C.L. Chen, S.W. Chou and C.C. Chen, "*Size-dependent magnetic parameters of fcc FePt nanoparticles: applications to magnetic hyperthermia*," Journal of Physics D: Applied Physics, Vol. 43, pp. 145002-145002-7 (2010)
47. K. Edinger, A. Gölzhäuser, K. Demota, C. Wöll and M. Grunze, "*Formation of Self-Assembled Monolayers of n-Alkanethiols on Gold: A Scanning Tunneling Microscopy Study on the Modification of Substrate Morphology*," Langmuir, Vol. 9, pp. 4-8 (1993)
48. E. Delamarche, B. Michel, C. Gerber, D. Anselmetti, H.-J. Güntherodt, H. Wolf and H. Ringsdorf, "*Real-Space Observation of Nanoscale Molecular Domains in Self-Assembled Monolayers*," Langmuir, Vol. 10, pp. 2869-2871 (1994)
49. G. E. Poirier and M.J. Tarlov, "*The c(4x2) Superlattice of n-Alkanethiol Monolayers Self-Assembled on Au(111)*," Langmuir, Vol. 10, pp. 2853-2856 (1994)
50. C. Schönenberger, J.A.M. Sondag-Huethorst, J. Jorritsma and L.G.J. Fokkink, "*What Are the 'Holes' in Self-Assembled Monolayers of Alkanethiols on Gold?*" Langmuir, Vol. 10, pp. 611-614 (1994)
51. M. Huijben, L.W. Martin, Y.-H. Chu, M.B. Holcomb, P. Yu, G. Rijnders, D.H.A. Blank and R. Ramesh, "*Critical thickness and orbital ordering in ultrathin* $La_{0.7}Sr_{0.3}MnO_3$ *films*," Physical Review B, Vol. 78, pp. 094413-1-094413-7 (2008)
52. M.H. Dishner, M.M. Ivey, S. Gorer, J.C. Hemminger and F.J. Feher, "*Preparation of gold thin films by epitaxial growth on mica and the effect of flame annealing*," Journal of Vacuum Science & Technology A, Vol. 16, pp. 3295-3300 (1998)
53. C. Nogues and and M. Wanunu, "*A rapid approach to reproducible, atomically flat gold films on mica*," Surface Science, Vol. 573, pp. L383-L389 (2004)
54. G. Herzog, S. Krause and R. Wiesendanger, "*Heat assisted spin torque switching of quasistable nanomagnets across a vacuum gap*," Applied Physics Letters, Vol. 96, pp. 102505-102505-3 (2010)

Acknowledgements

Concluding this report I would like to express my sincere gratitude to everyone who has supported me during my master's research project.

Before all else I extend my thanks to the members of my tutoring committee. Thanks to Wilfred van der Wiel and Tian Gang for the supervision of my work and for their generous support in all aspects of my research. Also thanks to Harold Zandvliet for being the external member of the committee and for showing me 'the ropes' of the student STM. I gratefully thank Michel de Jong for his theoretical support and constructive conversations, and Martin Siekman for his outstanding patience with all my practical issues with the STM equipment.

Furthermore I thank Ina Rianasari for her help in the chemical laboratory and Kim Wimbush for flame-annealing the gold substrates.

I also thank all the members of NanoElectronics for being a fantastic group of people whom I've spent countless enjoyable hours with, as well as all my fellow students from the NE and TST groups for making the student room an interesting place.

Finally I humbly honor our good God who has put my life on an awesome track, and continues to teach me what it means to be called His child forever.